

Supported heterogeneous catalyst of the copper oxide nanoparticles and nanozeolite for binary dyes mixture degradation: Machine learning and experimental design

Leandro Rodrigues Oviedo ^a, Daniel Moro Durzian ^a, Giane Engel Montagner ^a, Yolice Patricia Moreno Ruiz ^b, André Galemebeck ^b, Giovani Pavoski ^{c,d}, Denise Crocce Romano Espinosa ^c, Lissandro Dorneles Dalla Nora ^a, William Leonardo da Silva ^{a,*}

^a Applied Nanomaterials Research Group (GPNAp), Nanoscience Graduate Program, Franciscan University (UFN), Santa Maria, RS, Brazil

^b Academic Center of Vitória (CAV), Department of Fundamental Chemistry (DQF), Federal University of Pernambuco (UFPE), Recife, PE, Brazil

^c Polytechnical School of Chemical Engineering, University of São Paulo, São Paulo, SP, Brazil

^d Department of Materials Engineering, The University of British Columbia, Vancouver Campus, BC V6T 1Z4, Canada



ARTICLE INFO

Keywords:

Copper oxide nanoparticles
Heterogeneous photocatalysis
Machine learning
Nanozeolite

ABSTRACT

The present work aims to evaluate the photocatalytic activity of an alternative supported nanocatalyst (nANA@CuO-NPs) for a binary dye mixture (Crystal Violet and Methylene Blue, labeled CV:MB) under visible light and study to propose a model to predict the reaction pathway for the process. An experimental design (Central Composite Rotational Design with 3 factors and 2 levels – CCRD 2³) was proposed to evaluate the ideal condition of the CV/MB photodegradation and four machine learning algorithms (Decision Tree, Random Forest, Xtreme Gradient Boosting and Artificial Neural Network-Multilayer Perceptron) were used to predict the main degradation products. The supported nanocatalyst was characterized by X-ray diffraction (XRD), Attenuated Total Reflectance-Fourier Transform Infrared (ATR-FTIR) spectroscopy, N₂ porosimetry, Diffuse Reflectance Spectroscopy (DRS), Field Emission Gun – Scanning Electron Microscope (FEG-SEM), Scanning electron microscopy (SEM) with energy dispersive X-ray spectroscopy (EDX), zeta potential (ZP) and zero charge point (pHZCP). XRD diffractogram of the nANA@CuO-NPs showed the tenorite and analcime phases with crystallite size and microstrain ranging from 0.319 to 22.35 nm and 6.48–454 × 10⁻³. ATR-FTIR spectra indicated the presence of functional groups characteristic of copper oxide nanoparticles (CuO-NPs) and nanozeolite analcime (nANA) on the supported catalyst, confirming the impregnation method. SEM micrographs indicated a heterogeneous surface with clusters (CuO-NPs and nANA@CuO-NPs) and homogenous surface for nANA, while the EDX showed the nANA with Si/Al < 2 (low-silica nanozeolite) and nANA@CuO-NPs with the presence in the elemental composition of the catalytic support (nANA) and the photoactive phase (CuO-NPs). Supported nanocatalyst showed physio-chemical stability due to the electrostatic interactions (ZP = 51.5 ± 0.5 mV) and band gap energy (Eg) of the 1.67 eV allowing its applicability under visible radiation. XGB algorithm resulted in the best predictive model (R^2 equals 0.8106 and 0.9880 for training and testing, RMSE < 6.0), confirming the obtention of carbon dioxide (m/z = 44), water (m/z = 18) and low-molar mass compounds at the final of the binary dye mixture degradation reaction. The ideal condition for the by CCRD 2³ for the degradation of the dye mixture was [CV:MB] = 135 mg/L, [nANA@CuO-NPs] = 1 g/L and pH = 7 with 82.84 % (k = 0.0089 min⁻¹). Therefore, the synthesized nanocatalyst proved its good photocatalytic activity toward a cationic dye mixture of CV and MB dyes. Furthermore, this work confirms the potentiality of machine learning algorithms to develop predictive models for the elucidation of degradation reaction pathway of organic dyes.

* Corresponding author.

E-mail address: w.silva@ufn.edu.br (W.L. da Silva).

1. Introduction

In the textile industry, about 50,000 tons of synthetic organic dyes are produced and discharged as residue in wastewater, generating several adverse environmental impacts [1]. Most of these synthetic organic dyes are considered toxic, mutagenic, and teratogenic, being harmful to humans and aquatic biota [2]. In addition, these contaminants can cause respiratory diseases, eye, and skin irritation [3].

MB dye is extensively used in office supplies, in paper, pulp, wood and cotton industries, in the coloring of silk and wool, and in medicine (e.g., therapeutics and diagnostics procedures) [4]. CV and MB dyes are hydrophilic compounds, whose structure is made up of aromatic rings, making them poor optically, thermally and chemically stable, and quite low biodegradable [5,6]. The presence of MB and CV dyes in the wastewater compositions can lead to serious threats to the environment and harmful effects such as nausea, mental disorientation, diarrhea, sweating and breathing problems and even death to aquatic animals [7].

Advanced treatment processes have been used to adequately remove wastewater with dyes, highlighting the Advanced Oxidation Processes (AOPs) [8]. Among the AOPs, heterogeneous photocatalysis is based on the generation of reactive oxygen species (ROS) from water molecules and dissolved oxygen through the activation of a semiconductor (as supported nanocatalyst) under UV radiation or visible light, in which hydroxyl ('OH) and superoxide radicals ('O₂) react non-selective with the dye molecules [9]. Thus, when the semiconductor (catalyst) is photoactivated with energy equal to or greater than the band gap energy (E_g), electrons are promoted from the valence band (VB) to the conduction band (CB), generating the electron-hole pairs (e_{CB}⁻/h_{VB}⁺) [10]. Then, the e_{CB}⁻ reacts with oxygen molecules reducing them to superoxide radicals ('O₂'), while the h_{VB}⁺ reacts with water or hydroxide ion to generate hydroxyl radicals ('OH). 'O₂' and 'OH' reacts non-selectively with the react with organic pollutant molecules adsorbed onto the catalytic surface [11].

Heterogeneous photocatalysis has attracted much research mainly due to the sustainability, versatility, simplicity of the operation, and high efficiency in the removal of organic dyes from aqueous solutions by the mineralization of the organic matter to less toxic compounds (e.g., CO₂, H₂O, and trace short-chain organic compounds) [12].

Despite the high efficiency of heterogeneous photocatalysis, the electron-hole pair has a short lifetime and can migrate to the catalytic surface participating in the redox reaction or recombine resulting in heat loss, reducing the photodegradation of organic pollutants and limiting the process efficiency [13]. Thereafter, some strategies to reduce the e_{CB}⁻ and h_{VB}⁺ recombination are dropping and the immobilization of the semiconductor on an inert material called catalytic support, which helps in the adsorption of the target pollutants, which allows them to be near the catalytic surface where the radical species are generated, thus accelerating the reaction of the reactants with reactive species and avoiding the electron-hole pair recombination [14]. One more strategy is based on the creation of an electric field between the interface of the catalyst and the support, which avoids e_{CB}⁻/h_{VB}⁺ recombination by forcing them to move in opposite directions. In this sense, materials with strong or permanent electrical fields and good adsorption capacity, such as zeolites are attractive to be used as catalytic support [15].

Moreover, the nanocatalyst can be used doped with a photoactive phase, which increases its photocatalytic activity (with the reduction in the E_g) and hence the process efficiency [16]. Furthermore, alternative supported nanocatalysts have been encouraging new research on the photocatalytic degradation of dyes, especially due to their special properties (e.g., high surface area and porosity, band gap energy and wide range of light absorbance), and relatively low cost of production [17].

Copper oxide nanoparticles (CuO-NPs) are a p-type semiconductor strongly attractive to be used in dye photocatalytic degradation processes, especially due to their narrow band gap energy (E_g ~ 1.25–1.75 eV), low toxicity, and cost-effective when obtained by biogenic synthesis

[18]. Moreover, CuO-NPs have thermal stability, interesting optical-electronics properties (ferrimagnetic behavior), and ionic characters, with Cu⁺ and Cu²⁺ ions being participants of the organic compounds oxidation reactions or interact with the spin-restricted oxygen, generating more free radicals during the photocatalytic process [19]. Moreover, about 95 % of MB dye degradation was reported in the literature, in which the nanocatalyst CuO-NPs supported in nanozeolite X were used [20]. The green synthesis of CuO-NPs have been received special attention from the scientific community due to the low cost of production, wide availability of the stabilizing/reducing agents (such as plant extracts - *Camellia sinensis*, *Malva sylvestris*, *Calotropis procera* e *Acalypha indica*), safety and simplicity of the synthetic method as well as the textural, electric and optical proprieties of the obtained material [21]. In addition, green synthesis of CuO-NPs is preferable to conventional hydrothermal synthesis as it requires lower energy demand, relatively cheap precursors, and shorter chemical occurrence times [22].

To reduce time and experimental runs in batch-scale photocatalytic processes for organic dye removal from wastewater, the employment of computational tools has been used before the application of the process in industrial or full-scale. Additionally, the elucidation of the dye degradation reaction mechanism to develop a generic reaction pathway can emerge as an alternative and crucial tool before to scale-up. To mention a few, supervised machine learning algorithms based on decision tree-based models (e.g., Xtreme Gradient Boosting – XGB, and Random Forest – RF algorithms) and neural networks (Artificial Neural Network – ANN) should be employed and a good starting point to elucidate the main products of the degradation reaction and to predict the dye mineralization percent [23,24]. The great advantage of the use of machine learning algorithms is the capability to perform prediction for new data (i.e., unseen data by the algorithm or data out of the range of the experimental runs tested) after a suitable machine learning model is developed [25]. Thus, machine learning studies can be helpful to simulate new situations and achieve a better understanding of the process.

In this context, the present work aims to synthesize and characterize a novel supported heterogeneous catalyst (nANA@CuO-NPs) to be applied in the photocatalytic degradation of a binary mixture of synthetic organic dyes (CV and MB), meeting the principles of the Sustainable Development Goals (SDG), especially on clean water and sanitation, which aims to ensure the availability and sustainable management of water and sanitation for all. In addition, this work aims to propose a reaction mechanism for simultaneous CV and MB degradation through a generalized predictive model obtained from machine learning algorithms.

2. Material and methods

2.1. Nanozeolite synthesis

The analcime nanozeolite (nANA) was synthesized by hydrothermal method from (agro)industrial residues as precursors, according to the literature [26]. Thus, alum sludge (Al₂O₃ source) and rice husks (SiO₂ source) were added to 56 mL NaOH (2 mol/L, ACS reagent, ≥ 97.0 %, pellets, Sigma-Aldrich®) in a beaker under magnetic stirring (120 rpm/ 50 ± 2 °C for 20 min) to form a gel with molar composition of the 1.97Na: 1.0 SiO₂: 1.96 Al₂O₃: 62.25 H₂O. The mixture was transferred to a stainless-steel autoclave reaction coated with polytetrafluoroethylene (PTFE) heated at 180 °C for 6 h. After, the sample was filtered (filter Paper qualitative 45 mm), washed (distilled water and 70 % ethyl alcohol until pH ≈ 7), and dried (80 °C for 12 h). Then, the dried solid was calcined at 180 °C for 4 h (30 °C min⁻¹).

2.2. *Camellia sinensis* extract and copper oxide nanoparticles biosynthesis

Green tea leaves (*Camellia sinensis*) were collected in Santa Maria (29° 41' 29" S, 53° 48' 3" W) and dried at 25 ± 2 °C for 24 h (4 °C min⁻¹).

Table 1
CRD 2³ experimental design for CV:MB photodegradation.

	[CV:MB] (mg/L)	[nANA@CuO-NPs] (g/L)	pH
(-1.68)	26	0.16	2
(-1)	70	0.5	4
0	135	1.0	7
(+1)	200	1.5	10
(+1.68)	244	1.84	12

After, the dry material was grounded in a knife mill and sieved (#106 nm). Thus, 30 g of ground leaves were mixed with distilled water (30 min/250 rpm/25 ± 2 °C).

CuO-NPs were synthesized by biogenic synthesis [27]. For the reduction and nucleation steps, 200 mL of copper(II) chloride dihydrate (0.75 mol/L, CuCl₂·2H₂O, ACS reagent, ≥ 99.0 %, Sigma-Aldrich®) and 200 mL of the green tea extract (pH ≈ 6, 200 mg/L) were mixed under magnetic stirring (110 rpm, 65 ± 2 °C for 1.5 h). The solution was then cooled until to room temperature (25 ± 2 °C). The solution was cooled (25 ± 2 °C) and the precipitation formed was centrifuged (4500 rpm/20 min). For the stabilization step, the sample was dried at 60 °C for 4 h.

2.3. Synthesis of the supported heterogeneous nanocatalyst

The supported heterogeneous nanocatalyst (nANA@CuO-NPs) was synthesized by the impregnation method [28], where the CuO-NPs were used as photoactive phase and nANA as the matrix (catalytic support). Thus, CuO-NPs and nANA were mixed in a 0.025:1 ratio (in mass) with 100 mL of distilled water under magnetic stirring (110 rpm, 25 ± 2 °C for 1.5 h). After, the mixture was calcinated at 450 °C for 6 h (30 °C min⁻¹).

2.4. Characterization techniques

The pH_{ZP} was evaluated by 11-point assays, using NaOH (0.1 mol/L, ACS reagent, ≥ 97.0 %, pellets, Sigma-Aldrich®) and HCl (0.1 mol/L, ACS reagent, 37 %) for pH adjustments [29]. The thermal stability was evaluated by TGA analysis in a thermogravimetric balance (Shimadzu, model TGA-60/60H) with 20 mg of the sample under an air atmosphere (100 mL min⁻¹) and heating rate of 10 °C min⁻¹ to 900 °C.

DRS analysis was carried out in a JASCOV-670 spectrometer (λ = 200 – 800 nm) where the band gap energy (Eg) was measured by Eq. (1)–(3) and Kubelka-Munk method (Tauc plot – (F(R)hv)ⁿ versus hv, with $n = 1/2$, 1/3, 2/3 and 2) [30–32].

$$F(R) = \frac{(1 - R_{\infty})^2}{2R_{\infty}} \quad (1)$$

$$hv = \frac{1240}{\lambda} \quad (2)$$

$$R = \frac{1}{A} \quad (3)$$

Where: F(R) is the Kubelka-Munk function, R_{∞} is the reflectance (a.u.); hv is incident photon energy (eV), λ is wavelength associated to the maximum absorbance (nm).

The crystallinity and phases of the samples were investigated in a Brucker D2-Phase XRD diffractometer with $\lambda_{Cu-\alpha} = 0.15418$ nm with 2θ ranging from 5 to 70° and acceleration tension of 30 mA. The average crystallite size and interplanar distance were evaluated from Scherrer equation (4), Bragg's equation (5), and Williamson-Hall model (6) [33].

$$dc = \frac{K^*\lambda}{\beta^*\cos(2\theta)} \quad (4)$$

$$d = \frac{\lambda}{2^*\sin(\theta)} \quad (5)$$

$$dc = \frac{0.89^*\lambda}{\beta^*\cos(\theta) - 4\varepsilon^*\sin(\theta)} \quad (6)$$

Where: K is a shape factor which depends on the type of particle (0.94 for spherical particles); θ is the Bragg angle, in degrees and β corresponds to the full width at half maximum height of the diffraction peak.

The identification of the functional groups was obtained by the Fourier Transform Infrared Spectrum (FTIR) in a Perkin Elmer Spectrum Frontier with ATR (attenuated total reflectance) accessory in transmittance mode ranging from 4000 and 450 cm⁻¹ (with 45 scans and 4 % resolution). For N₂ porosimetry, the equipment (Gemini VII 2375 Surface Area Analyzer Micrometrics) was used (P/P⁰ = 0.0–1.0) and the textural properties (S_{BET}, D_p an V_p) were evaluated by the Brunauer-Emmett-Teller (BET) and Barret-Joyner-Halenda (BJH) methods. Field Emission Gun Scanning Electron Microscopy (FEG-SEM) was used to determine the morphological characteristic in a MIRA3 (TESCAN, Czech Republic). The average particle size was measured using ImageJ® software (NIH, USA), where 200 random points were selected. Malvern-Zetasizer® (model nano ZS, ZEN3600 -United Kingdom) was used to determinate the surface charge by ZP. For the elemental composition, EDX was used in a X PHENO (model PROX 2020) operating at 15 kV and full backscattered electron.

2.5. Camellia sinensis extract flavonoids characterization

The substances present in the green tea extract were carried out by total flavonoid content (TFC) and total phenolic content (TPC) [34,35]. For the TPC test, 0.5 mL of the *Camellia sinensis* extract was diluted in methanol (ACS reagent, ≥ 99.8 %, Sigma-Aldrich®) followed by the addition of 0.5 mL Folin-Ciocalteu reagent (ACS reagent, ≥ 98.0 %, Sigma-Aldrich®) (1:10 v v⁻¹). After 5 min in the dark, 1.0 mL of 7.5 % Na₂CO₃ (ACS reagent, ≥ 99.5 %, Sigma-Aldrich®) was added and mixed at 50 °C under magnetic stirring (110 rpm/5 min) and cooled at room temperature (25 ± 2 °C). The absorbance was measured against the prepared reagent blank at 760 nm using a double-beam UV/Vis spectrophotometer. Thus, the concentration of total phenolic compounds in the extract was expressed as milligrams of gallic acid equivalent (GAE) per 100 g sample (mg/g). All the samples were analyzed in triplicate.

For the TFC, 0.5 mL of the extract was added in 10 mL of the test tube containing 2 mL of distilled water. To each test tube, 0.15 mL of 5 % NaNO₂ (ACS reagent, ≥ 97.0 %, Sigma-Aldrich®) was added. After 5 min of incubation, 0.15 mL 10 % AlCl₃ (reagent grade, 98 %, Sigma-Aldrich®) was added. After 1 min, 1 mL of NaOH (1 mol/L, ACS reagent, ≥ 97.0 %, pellets, Sigma-Aldrich®) was added and the volume was adjusted to 5 mL with distilled water. After 10 min, the absorbance of the resulting solution was measured at 510 nm. Catechin was used as the standard to express the total flavonoid content of samples as mg catechin equivalent per 100 g of sample (mg/g). All the samples were analyzed in triplicate.

2.6. Experimental design

To determine the ideal condition for the heterogeneous photocatalysis, a design of experiments, the CCRD 2³, was carried out. The CCRD 2³ selects a response variable, which is dependent on the input variable and through statistical p-value, Pareto chart and surface response find the parameters that affect statistically the response of the model. Thus, the dye mixture concentration ([CV:MB]), nanocatalyst concentration ([nANA@CuO-NPs]) and pH were selected as independent variables and dye photodegradation percentage (%R) was selected as the response or dependent variable, according to the Table 1.

The experimental design showed 70 and 200 mg/L for inferior and superior limits of the dye concentration, which is the concentration range commonly found in textile industries, according to the literature presenting textile wastewater characteristics [36]. Additionally, the

Table 2

Technical details of machine learning algorithms.

Algorithm	Algorithm parameters	Equations	Reference
Decision Tree (DT)	Tree maximum depth*: 5, 10, 15, 20, 25 m Number of splits per tree: 5, 10, 12, 15 Performance measured by minimizing the mean squared error $R(T)$, according to Eq. (10)	$R(T) = \frac{1}{N} \sum_{n \in T} \sum_{i \in T} (y_i - \hat{y}_i)^2 (10)$ <p>Where: $R(T)$ = Expected value of the sum of mean squared errors using a constant as a predictive model; N is the number of nodes used in the decision/pattern recognition in the data (one node is equivalent to one leaf of the decision tree); y_i = observed value obtained experimentally; \hat{y}_i = predicted value obtained from the model; t = identifier of each node, T = mean squared error between the observed and the predicted values (response).</p>	[38]
Multilayer Perceptron Artificial Neural Network (MLP-ANN)	Neural network structure: $m:n:k$, where m is the number of input data (independent variables), n is the number of neurons in the hidden layer, which is responsible for processing the data Main node function: summation/activation function used in each node (Eq. 11), associated with reLu (Eq. 12), logistic (Eq. 13) and hyperbolic tangent (Eq. 14) functions Weight optimization function: lbfgs, Adam**	$\varphi = \sum w_n \bullet x_n + b_k (11)$ $f(\varphi) = (0, x_{\max}) (12)$ $f(\varphi) = \frac{1}{1 - e^{-\varphi}} (13)$ $f(\varphi) = \frac{2}{1 + e^{-2\varphi}} - 1 (14)$ <p>Where: φ = transfer function; x_n = n-th neural network node; w_i = weight associated with the nth neuron x_n; b_k = bias (error associated with the prediction model); x = maximum value predicted by the ANN algorithm, using the ReLu function</p>	[39]
Random Forest (RF) and Xtreme Gradient Boosting (XGB)	Tree maximum depth: 5, 10, 15, 20, 25 m. Number of decision trees tested: 25, 50, 75, 100 Performance measured by minimizing the mean squared error $R(T)$, as defined in DT algorithm	<p>Eq. (10) but using more than one decision tree, with n-repartitions of the trees, deity in a group of k-elements, generating a particular answer (decision i, j, k). The algorithms use optimization functions that guarantee greater computational power, fast convergence to the optimal value predicted by the algorithm and less probability of overfitting</p> <p>Response = average of the decisions of the n-groups made up of k-trees</p>	[40]

$cv = 5$ for all algorithms tested | * Parameter associated with the learning rate of the algorithm | **Limited-memory Broyden–Fletcher–Goldfarb–Shanno function. | *** Increasing the lambda parameter (λ) disproportionately reduces the influence of small leaves (those with few observations), having only a minor impact on larger leaves (those with high number of observations).

nanocatalyst concentration and pH range from 0.5 – 1.5 g/L and 4–10, respectively, to verify the effect of these parameters for the CV and MB degradation by heterogeneous photocatalysis.

2.7. Photocatalytic assay

Heterogeneous photocatalysis test was carried out using a dyes mixture (CV:MB) as a target molecule in a slurry reactor under visible irradiation (Empalux® Bulb LED Lamp, 50 Watt Halogen Equivalent with 600 W m⁻² and as the maximum radiations and wavelength ranging from 275 to 950 nm) in two steps; (a) in dark condition: adsorption of dyes molecules onto the catalytic surface without irradiation (~60 min), and (b) photocatalytic degradation of the dyes: under visible radiation and a distance of about 20 cm from the LED lamp and sample, aliquots (~2 mL) were collected at time 0, 15, 30, 45, 60, 75, 90, 120, 150, and 180 min, filtrated ($\phi = 0.45 \mu\text{m}$) and diluted (1:15 v v⁻¹). The photodegradation percentage of the dyes (%R) was evaluated in a UV-vis spectrophotometer at $\lambda = 590$ nm (CV) and $\lambda = 663$ nm (MB), according to Eq. (7).

$$\%R = y_i A_i + y_j A_j \quad (7)$$

Where: y_i and y_j are the molar fractions of CV and MB dye, respectively; A_i is the absorbance read at $\lambda = 590$ nm; A_j is the absorbance read at $\lambda = 663$ nm. The molar fraction of the dyes was set to $y_i = y_j = 0.5$, i.e., an equimolar mixture.

2.8. Photodegradation kinetics

A kinetic study of the photocatalytic degradation of the dyes mixture was performed using the Langmuir-Hinshelwood kinetic model simplified to dilute solutions, according to the Eqs. (8) and (9) [37].

$$(-r_i) = -\frac{dC_i}{dt} = \frac{k_s * K * C_i}{1 + K * C_i} \quad (8)$$

$$C_{i,t} = C_{i,0} * e^{-k*t} \quad (9)$$

Where: $(-r_i)$ is the reaction rate (mol/L min⁻¹), K is the adsorption

coefficient of the compound to be degraded (L mg⁻¹), k_s is the apparent constant of reaction (mol/L min⁻¹), $C_{i,0}$ is the initial dye concentration (mg/L), C_i is dye concentration at time t (mg/L), t is the illumination time (min) and k is the apparent rate of the pseudo first-order reaction (min⁻¹).

2.9. Reuse of the nanocatalyst

The effect of the nANA@CuO-NPs recycling was carried out using the ideal condition by CCRD 2³ after 6 cycles of photodegradation. Thus, after each cycle (after 180 min under visible irradiation), the binary dye mixture was centrifuged (3500 rpm for 20 min) and the solid (nanocatalyst) was carefully separated and reintroduced in the slurry reactor. The photodegradation percentage of the dyes was measured for each cycle (Eq. (6)).

2.10. Dye degradation reaction pathway

To investigate a reaction mechanism for the CV:MB photodegradation, ML algorithm was used to propose a generalist equation. Thus, four models (Decision Tree - DT, Random Forest – RF, Xtreme Gradient Boosting – XGB and Multilayer Perceptron Artificial Neural Network – MLP-ANN algorithms) were used to predict the main degradation products. 5-fold cross validation ($cv = 5$) was used for all algorithms. The algorithms were encoded and compiled in Python 3.1 (version Open Source) in Google Colaboratory, using libraries scikit-learn for tree-based machine learning models and metrics evaluation, whereas tensorflow and keras were used to construct and run the artificial neural network, respectively. The input variables (pH, reaction time, nanocatalyst and dye concentration) and the response (mass-charge ratio, m/z) of the ML algorithm were only data reported by GC-MS from scientific works that used heterogeneous photocatalysis in the MB and CV degradation under visible irradiation, using metallic supported heterogeneous nanocatalysts (excluding the CCRD data of this work, once did not involve GC-MS analysis). The dataset (file Degradation_reaction_pathway.xlsx) was provided in GitHub (<https://github.com/LeandroOviedo/Machine-and-Deep-Learning>), where 20 % of the

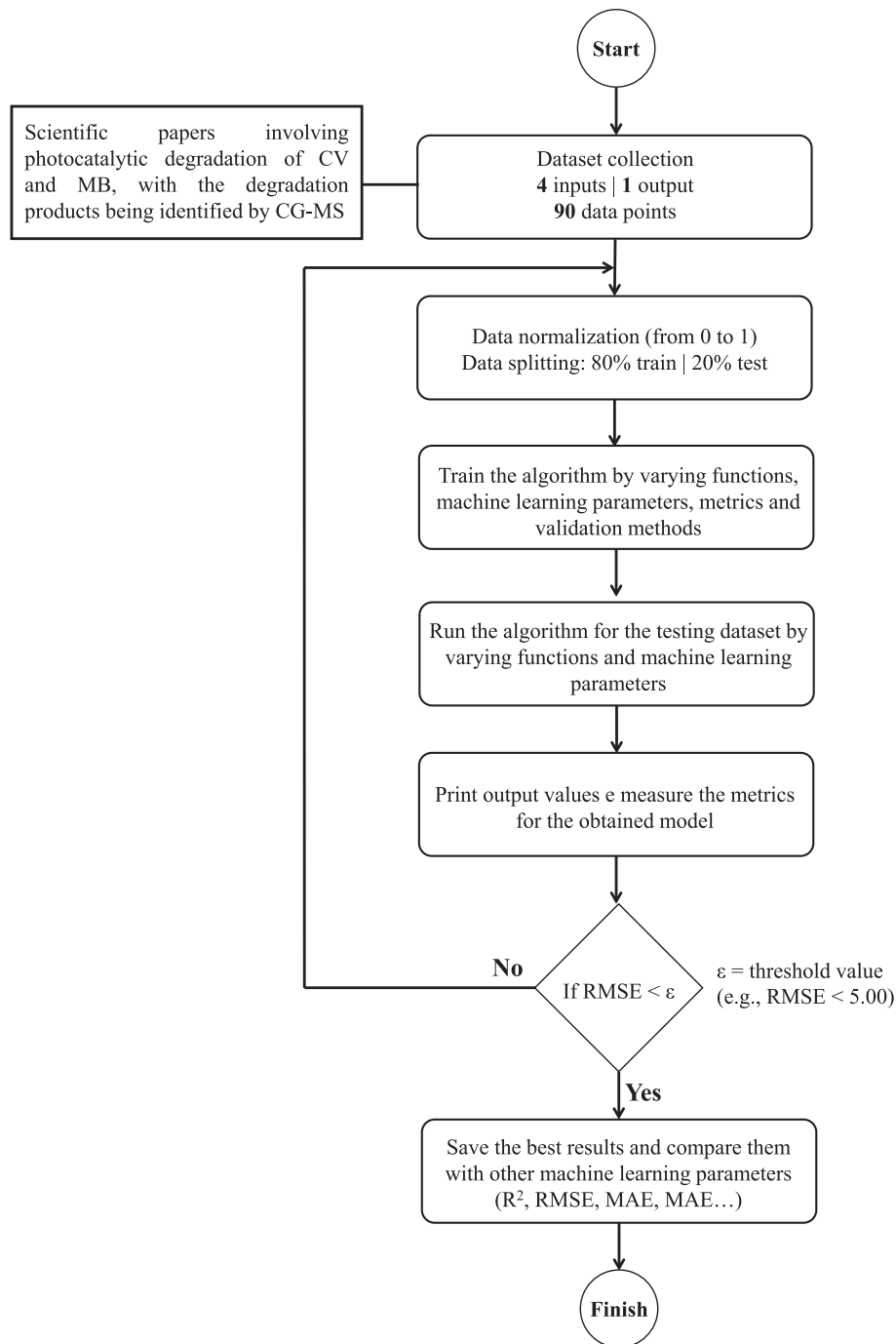


Fig. 1. Flowchart of the structuration and compilation of the algorithm in the machine learning study.

dataset were used for testing. Data were normalized with the importation and use of the preprocessing and Standard Scaler functions from scikit-learn library, using the command MaxMinScaler to normalize data in the range between 0 and 1. Table 2 shows the configurations of each ML algorithm used in this work and Fig. 1 informs the process flowchart of the algorithm structure and compilation.

3. Results and discussion

3.1. Characterization of the nANA@CuO-NPs

Fig. 2 shows the XRD diffractograms, where nANA@CuO-NPs showed characteristic peaks of the analcime phase ($\text{Al}_2\text{H}_4\text{Na}_2\text{O}_{14}\text{Si}_4$ -

COD 9008387) at 15.73° ($d = 5.64 \text{ \AA}$), 18.16° ($d = 4.88 \text{ \AA}$), 24.29° ($d = 3.66 \text{ \AA}$), 25.86° ($d = 3.44 \text{ \AA}$), 30.52° ($d = 2.92 \text{ \AA}$), 31.84° ($d = 2.81 \text{ \AA}$), 33.15° ($d = 2.70 \text{ \AA}$), 35.58° ($d = 2.52 \text{ \AA}$), 38.77° ($d = 2.32 \text{ \AA}$), 47.53° ($d = 1.91 \text{ \AA}$), 48.55° ($d = 1.87 \text{ \AA}$), 52.40° ($d = 1.74 \text{ \AA}$), 57.66° ($d = 1.59 \text{ \AA}$), 61.56° ($d = 1.50 \text{ \AA}$), 65.72° ($d = 1.42 \text{ \AA}$) and 69.06° ($d = 1.36 \text{ \AA}$) and the tenorite phase (CuO - COD 1011148) at 35.74° ($d = 2.51 \text{ \AA}$), 38.72° ($d = 2.32 \text{ \AA}$), 61.66° ($d = 1.50 \text{ \AA}$), 65.92° ($d = 1.42 \text{ \AA}$) and 68.05° ($d = 1.38 \text{ \AA}$), which obtained good agreement with the XRD standard of nanozeolites and copper nanoparticles in the literature [41,42]. Moreover, it was possible to verify a decrease in the intensity of CuO-NPs, indicating its incorporation in the catalytic support (nANA) confirming the impregnation success (nANA@CuO-NPs) [43]. It is noteworthy that the nANA@CuO-NPs showed lower average crystallite diameter (d_c =

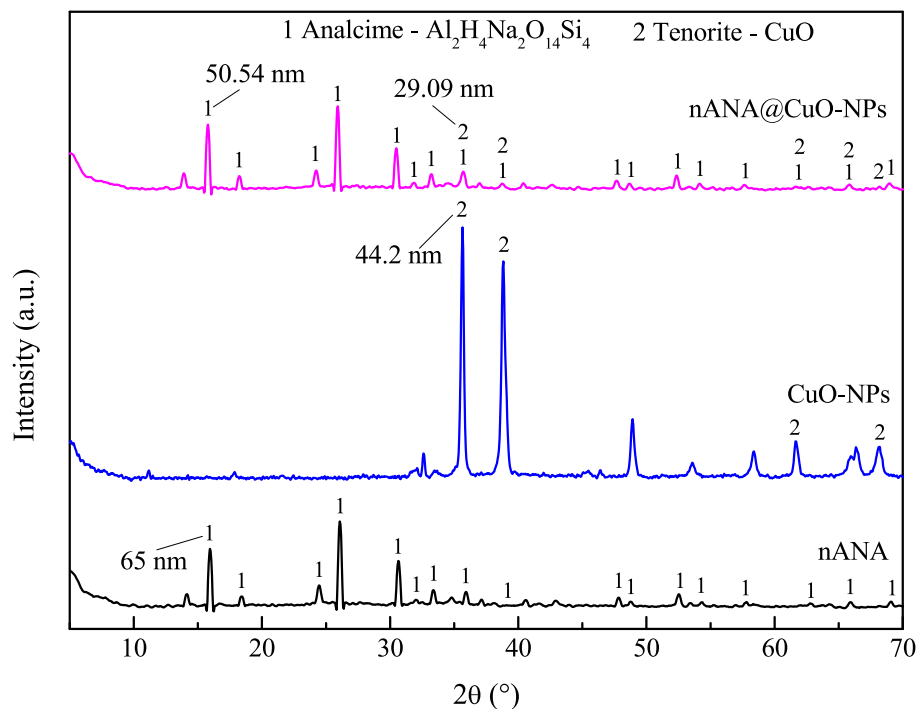


Fig. 2. XRD diffractograms of the nANA, CuO-NPs and nANA@CuO-NPs.

Table 3
Crystallite size and microstrain evaluation by Williamson-Hall method.

Sample	Crystallite diameter, D_c (nm)	Microstrain (ϵ) $\times 10^{-3}$
CuO-NPs	22.3	6.48
nANA	4.42	22.6
nANA@CuO-NPs	0.319	454

50.54 nm and $d_c = 29.09$ nm analcime phase and tenorite, respectively) in relation to the crystalline phases of both separate materials (nANA – 65 nm and CuO-NPs – 44.2 nm) possibly due to the temperature of calcination used in the supported heterogeneous nanocatalyst synthesis (450 °C for 6 h) promoting an increase in the coalescence processes of the particles and hence the reorganization of the atoms.

In parallel, the crystallite diameter and microstrain of nANA, CuO-NPs, and nANA@CuO-NPs were evaluated by the Williamson-Hall

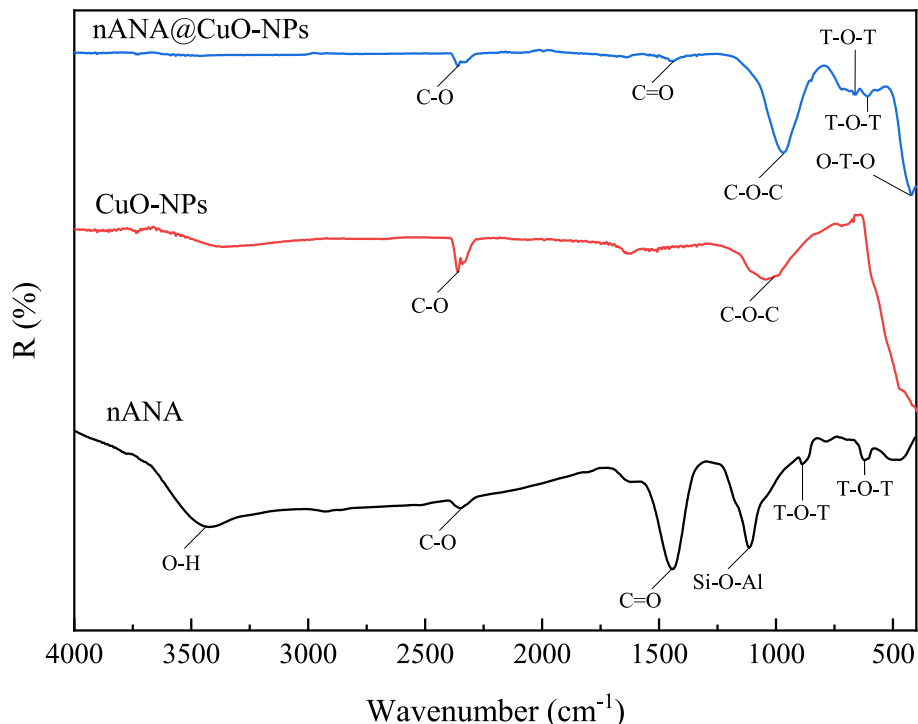


Fig. 3. ATR-FTIR spectra of the nANA, CuO-NPs and nANA@CuO-NPs.

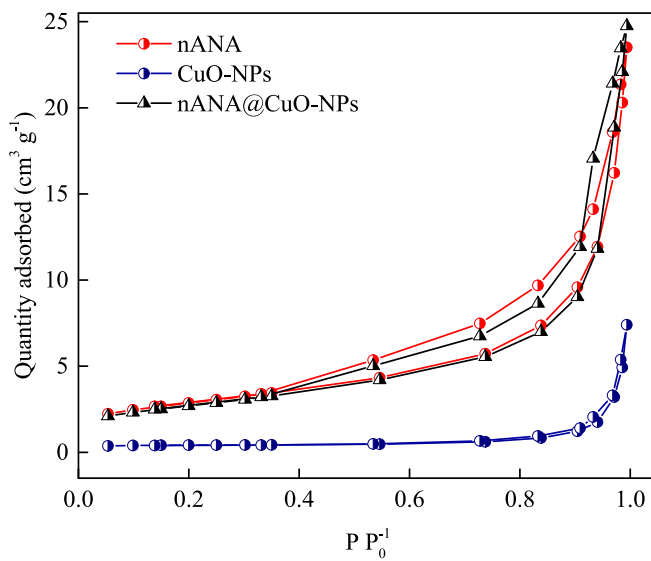


Fig. 4. N_2 adsorption/desorption isotherms of the nANA, CuO-NPs and nANA@CuO-NPs.

Table 4

Textural and surface properties of nANA, CuO-NPs and nANA@CuO-NPs.

Samples	S_{BET} (m^2/g)	D_p (nm)	V_p ($cm^3 g^{-1}$)	ZP (mV)
CuO-NPs	2 ± 0.05	37.1 ± 1.8	0.05 ± 0.001	-29.9 ± 1.3
nANA	16 ± 0.7	12.9 ± 1.0	0.03 ± 0.001	-29.2 ± 1.4
nANA@CuO-NPs	15 ± 0.8	14.7 ± 0.7	0.004 ± 0.004	-51.5 ± 0.5

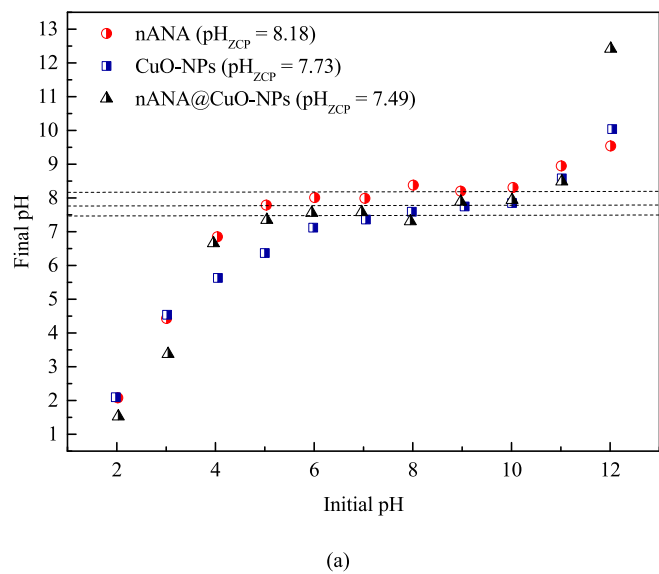
method (Table 3).

According to Table 3, the crystallite diameter reduced significantly when the CuO-NPs and nANA were combined, probably due to an increase in the atomic packing factor of the nANA@CuO-NPs. Moreover, due to the high organization of the zeolitic framework of nANA, lesser D_c than CuO is expected. In addition, the decrease in the microstrain values of the samples as the crystallite diameter increases reveals that the measurements performed by Williamson-Hall methods were coherent and precise, once this pattern is observed in the literature [44].

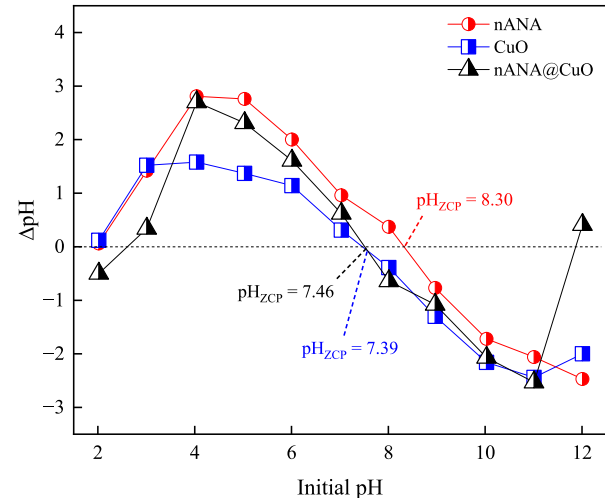
Fig. 3 shows the ATR-FTIR spectra of the nANA, CuO-NPs, and nANA@CuO-NPs, where were identified the respective functional groups for nANA@CuO-NPs sample: (a) at 2364.2 cm^{-1} : C–H stretching vibrational of the methylene group, (b) at 1446.4 cm^{-1} : stretching vibrational of the carboxyl group ($\text{C}=\text{O}$) originating from the sludge, (c) at 1043.3 cm^{-1} : C–O stretching vibrational of ester saturated from the plant extract, (d) at 587 cm^{-1} : stretching vibrations associated to double rings of sodalite cages, (e) at $500\text{--}650\text{ cm}^{-1}$: external bending vibrations of double rings of the tetrahedra framework, T–O–T, where T = Al or Si and (f) at 462 cm^{-1} : bending vibration of O–T–O (where T = Si or Al). [45]. Thus, nANA@CuO-NPs showed silicates, aluminates, and organic compounds as the main functional groups (mainly due to the biosynthesis of CuO-NPs). Moreover, the asymmetric stretching at $1250\text{--}950\text{ cm}^{-1}$, 979 cm^{-1} , and $720\text{--}650\text{ cm}^{-1}$ on nANA can be associated with internal stretching vibrations (symmetric and asymmetric) of T–O–T (where T = Si or Al) [46].

Fig. 4 shows the adsorption/desorption isotherms of the nANA, CuO-NPs and nANA@CuO-NPs, where showed IV-A type isotherms with H3-type hysteresis, typically found for mesoporous materials with slit-type pores [47].

Table 4 shows the textural properties of the samples, where it is observable that CuO-NPs showed the smallest specific area (S_{BET}), but the highest pore diameter (D_p) and pore volume (V_p) due to the calcination temperature used in the synthesis, which is expressively higher ($T = 450\text{ }^\circ\text{C}$) than the temperature of the synthesis of nANA ($T =$



(a)

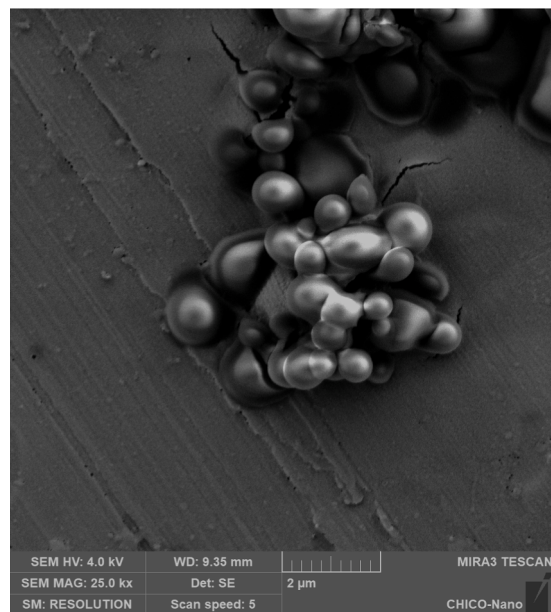


(b)

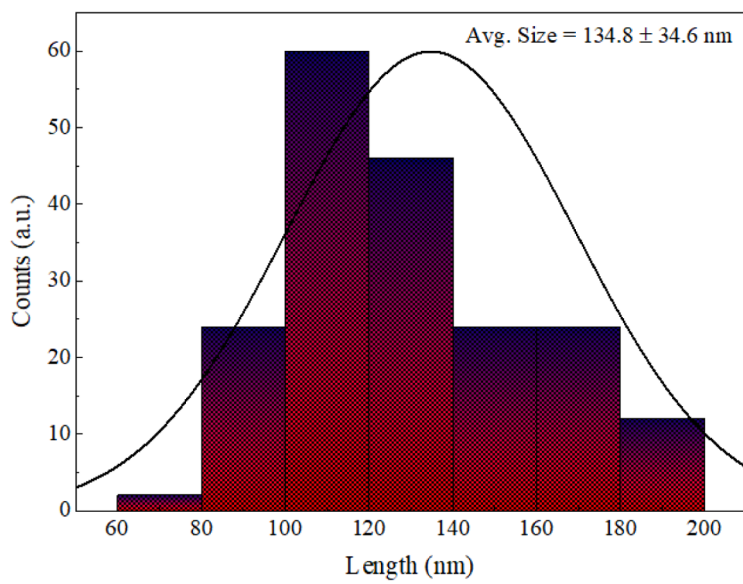
Fig. 5. pH_{ZCP} of the nANA, CuO-NPs and nANA@CuO-NPs evaluated from initial pH versus final pH (a) and (b) initial pH versus ΔpH .

$180\text{ }^\circ\text{C}$), being the CuO-NPs more susceptible to coalescence phenomenon. However, the observable S_{BET} for nANA@CuO-NPs is attributed to the nanozeolite presence in the composition of the supported nanocatalyst, whose S_{BET} measured was remarkably close to the nANA surface area. Moreover, nANA and nANA@CuO-NPs showed mesoporous structure and CuO-NPs approximated to microporous materials. V_p is strongly associated with the photocatalytic activity of the nanomaterials, in which the following tendency has been observed in scientific reports: the higher V_p indicated higher the photocatalytic activity of the nanomaterial, due to the higher space to receive and accommodate the molecules of the contaminants (e.g., dye molecules). However, in this study, owing to the low values for S_{BET} and V_p of the nanocatalyst, the value of ZP and the band gap energy (E_g), discussed in the following sections, probably were responsible for the high photocatalytic activity of the nANA@CuO-NPs. Thus, the ZP ranged from 29.90 to 51.53 mV (in the module) for the samples, suggesting good physicochemical stability due to electrostatic factors.

Fig. 5(a) and 5(b) inform the zero charge point (pH_{ZCP}) of the samples. Thus, pH_{ZCP} 8.18, 7.73, and 7.49 were evaluated for nANA, CuO-NPs, and nANA@CuO-NPs, respectively. At pHs lower than pH_{ZCP} , the



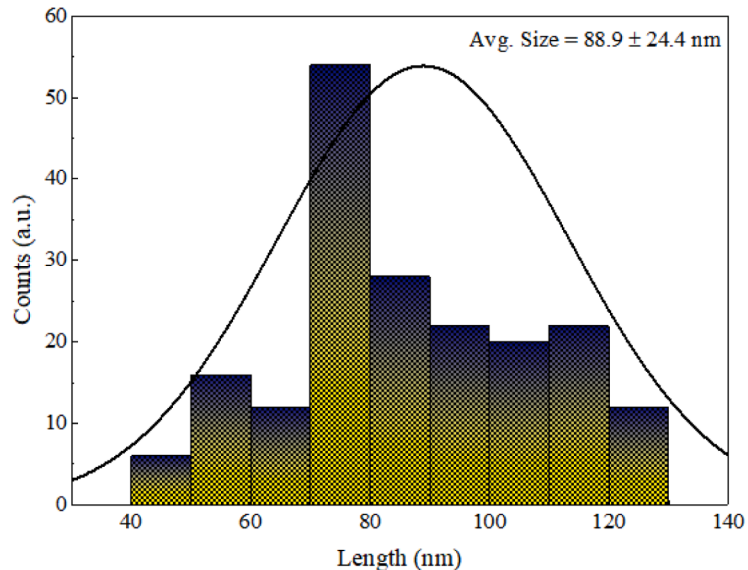
(a)



(b)



(c)



(d)

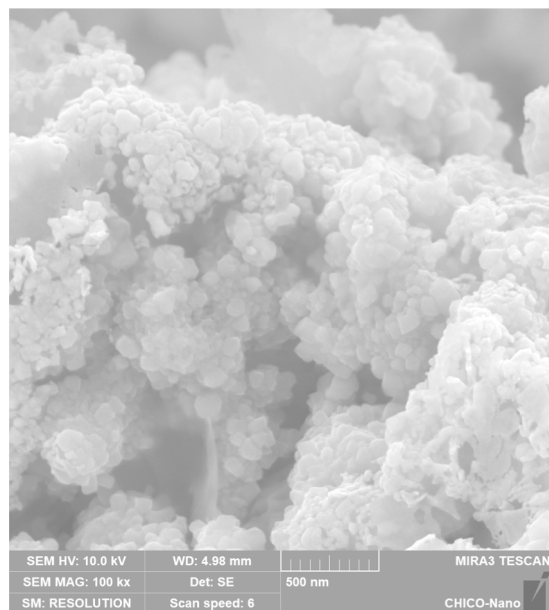
Fig. 6. FEG-SEM micrographs and particle size distribution curve to (a-b) CuO-NPs, (c-d) nANA and (e-f) nANA@CuO-NPs.

material surface charge is protonated being positive, whereas at pH higher than pH_{ZCP} its surface charge is deprotonated, and hence negative [48]. At these pHs, the samples showed little or no effect on the pH and electric charges in the solution. The catalytic support nANA showed higher pH_{ZCP} than CuO-NPs and nANA@CuO-NPs probably due to the chemical composition of the nanozeolite, comprised of Al and Si atoms, connected through O atoms. Moreover, similar values for zero charge point ($pH_{ZCP} \sim 8$) were found in the literature for low-silica nanozeolites, which agreed with the pH_{ZCP} measured in this work [49]. Regarding the CuO-NPs (pH_{ZCP} 7.73), it was observable that the pH_{ZCP} reduced to 7.49, probably due to the interaction of the Al—O—Al groups of the nanozeolite, which turns the nanomaterial surface charge more negative at neutral pH [50]. Thereafter, it expected that at pH higher

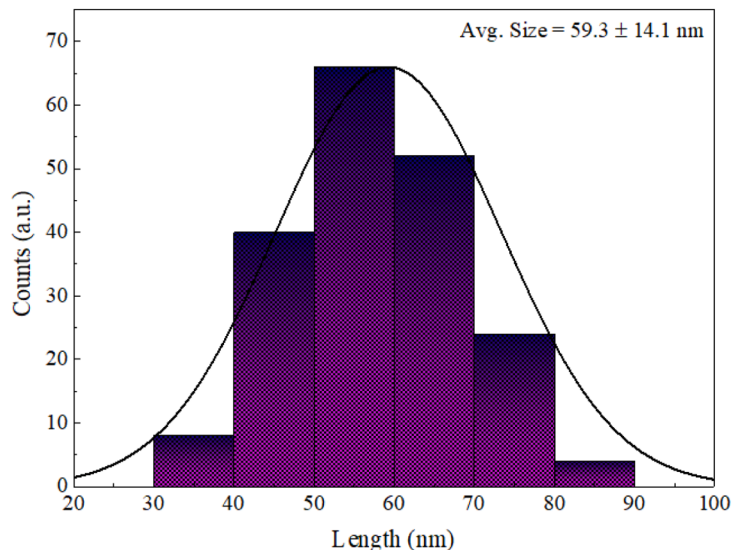
than 7.49, nANA@CuO-NPs showed a strong influence of the positive charges, whereas at pH lower than 7.49 the negative charges should interact with the more positive surface charge of the supported nanocatalyst [51]. Thus, the adsorption of the cationic dye molecules should be higher at neutral and alkaline pH, and lesser at strongly acidic pHs (due to the electrostatic repulsion between dye molecules and positive surface charge of the nanocatalyst).

Fig. 6 shows the results of the morphologic analysis of the nanocatalyst and its counterparts obtained by FEG-SEM.

SEM micrographs shown in Fig. 6(a) and 6(e) revealed a heterogeneous surface with clusters of CuO-NPs and nANA@CuO-NPs, and a homogenous surface for nANA (Fig. 6c). According to Fig. 6(b) and 6(d), the average particle size was 134.8 nm and 88.9 nm for CuO-NPs and



(e)



(f)

Fig. 6. (continued).

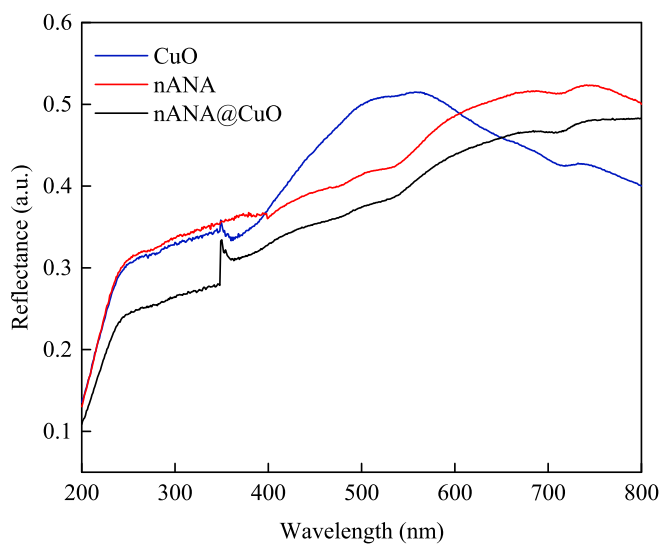


Fig. 7. DRS spectra of the CuO-NPs, (b) nANA, (c) nANA@CuO-NPs samples.

nANA, respectively. Fig. 6(f) shows the average particle size of the supported heterogeneous catalyst around 59.3 nm, being higher than CuO-NPs and lower than nANA due to the agglomeration of these nanomaterials.

Fig. 7 shows the reflectance and absorption edges for the catalyst and its counterparts, which is useful for determining the electronic and

optical properties. The band gap energies (E_g) measured by the Kubelka-Munk function ($F(R)$) for CuO-NPs, nANA, and nANA@CuO-NPs were informed in Table 5. CuO-NPs is the active substance of the nanocatalyst nANA@CuO-NPs, and hence, the optical properties of light absorption, E_g , and reflectance should be carefully understood. Thus, according to Fig. 7, the reflectance of the CuO-NPs is suppressed with their incorporation into the catalytic support (nanozeolite). Furthermore,

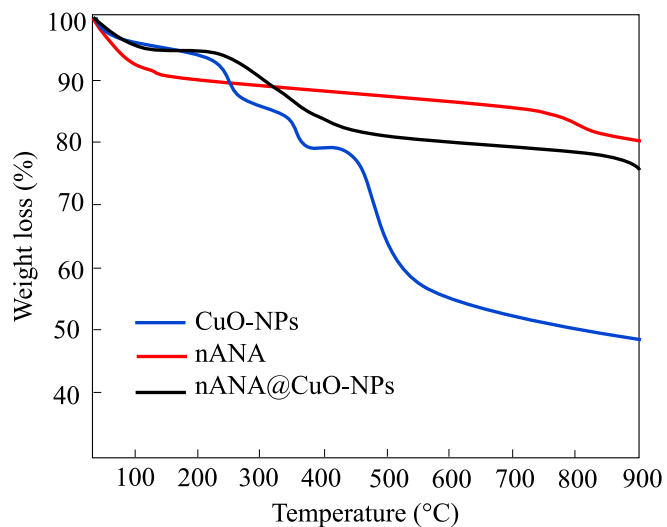


Fig. 8. TGA thermograms of the CuO-NPs, nANA and nANA@CuO-NPs.

Table 5

Band gap energies generated from Kubelka-Munk the nanocatalyst and its counterparts.

Sample	E_g (eV) ($n = 1/3$) Indirect forbidden transition	E_g (eV) ($n = 1/2$) Indirect allowed transition	E_g (eV) ($n = 2/3$) Direct forbidden transition	E_g (eV) ($n = 2$) Direct allowed transition	Absorption edge λ (nm)	E_g (eV)
nANA	1.26	1.25	1.28	1.28	747	1.65
CuO-NPs	1.55	1.54	1.66	1.61	557	2.22
nANA@CuO-NPs	1.05	1.10	1.05	1.07	741	1.67

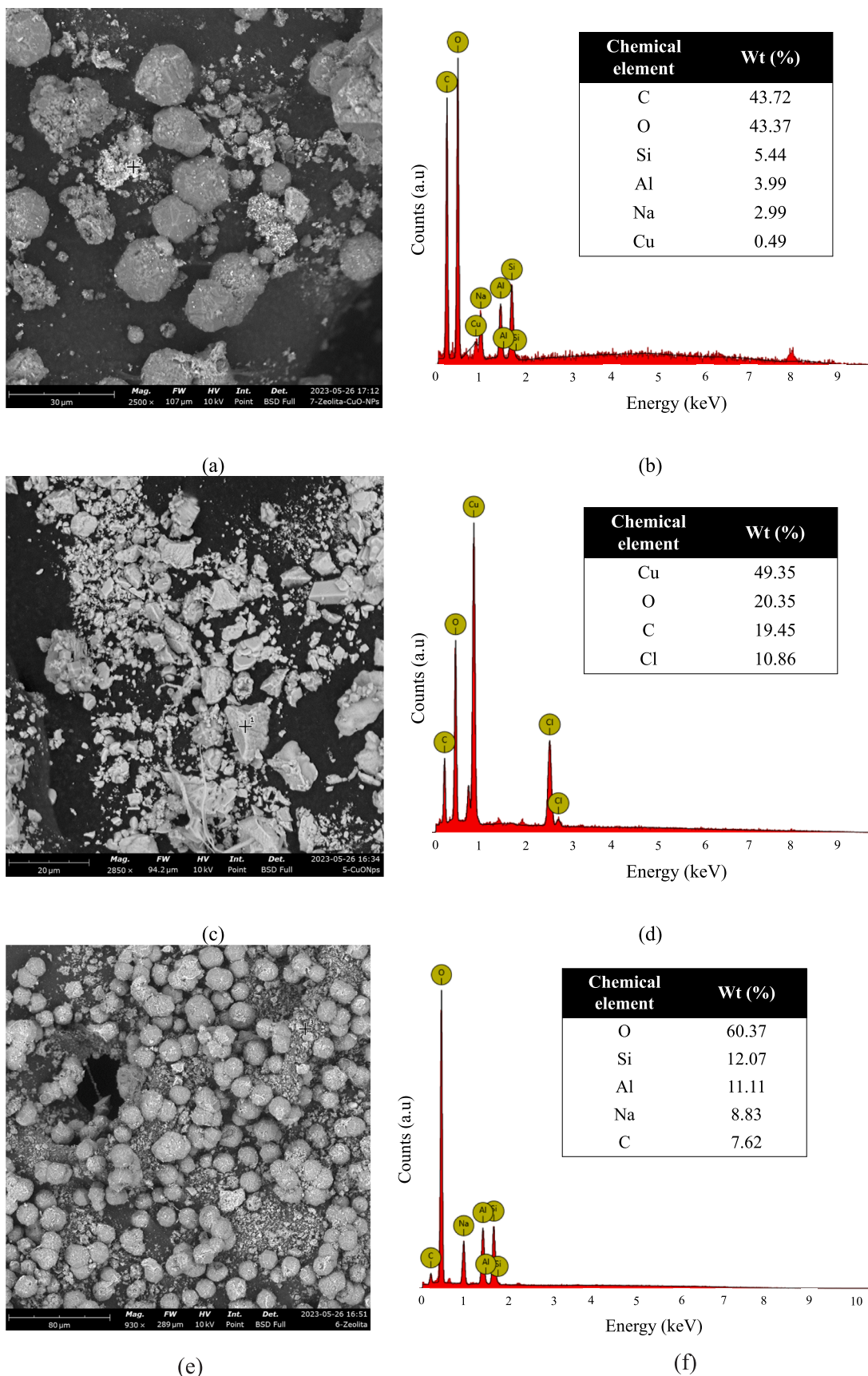


Fig. 9. SEM micrographics and EDX results of (a-b) CuO-NPs, (c-d) nANA, (e-f) nANA@CuO-NPs.

Table 6

Flavonoids and total phenols evaluated for the *Camellia sinensis* extract.

Flavonoids content (mg/g)		Total phenols (mg/g)	
17.45 ± 0,48		18.52 ± 0,57	

Table 7

CCRD 2³ results for CV:MB photodegradation.

Run	[dye] (mg/L)	[nANA@CuO-NPs] (g/L)	pH	%R (CV)	%R (MB)	%R
1	200	0.5	10	79.95	40.74	57.99
2	135	1	2	56.99	63.70	60.75
3	135	1	7	70.95	82.28	77.29
4	244.32	1	7	36.82	52.24	45.46
5	135	1	12	81.15	38.46	57.24
6	200	1.5	10	48.04	53.92	51.33
7	70	1.5	4	68.36	73.06	70.99
8	135	0.16	7	79.13	74.45	76.51
9	135	1	7	78.50	86.25	82.84
10	135	1	7	74.24	82.40	78.81
11	135	1.84	7	67.39	75.86	72.13
12	70	0.5	4	52.63	54.17	53.49
13	200	0.5	4	44.84	62.53	54.75
14	200	1.5	4	33.44	43.47	39.06
15	70	0.5	10	36.36	40.89	38.90
16	25.68	1	7	46.81	39.39	42.65
17	70	1.5	10	53.69	48.04	50.53

Table 8

Sum of Squares (SS), degrees of freedom (df), mean square error (MS), F_{CAL} (calculated degrees of freedom), F_{TAB} (degrees of freedom tabulated) and determination coefficient (R²).

Factor	SS	df	MS	F _{CAL}	F _{TAB}	R ²
[CV:MB]	2.697	1	2.697	19.3	3.68	0.9472
[CV:MB] ²	2071		2071			
[nANA@CuO-NPs]	0.024		0.024			
[nANA@CuO-NPs] ²	91.18		91.18			
pH	47.52		47.52			
pH ²	778.63		778.63			
[CV:MB]*[nANA@CuO-NPs]	331.25		331.25			
[CV:MB]*pH	319.84		319.84			
[nANA@CuO-NPs]*pH	1.248		1.248			
Error	171.0	7	24.43			
Total Sum of Squared Error	3237	16	—			

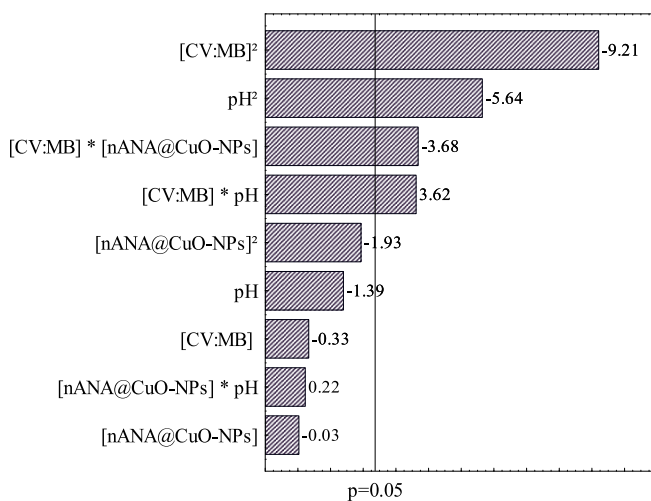


Fig. 10. Pareto chart for the nANA@CuO-NPs nanocatalyst experimental design.

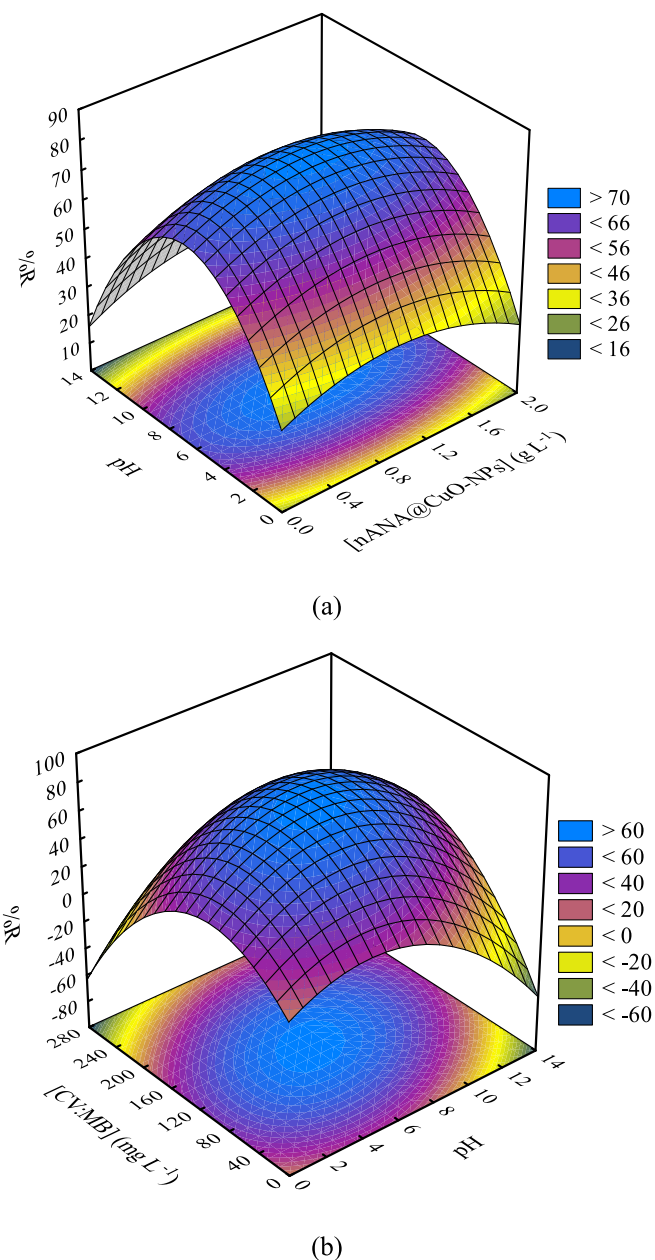


Fig. 11. 3D surface response for CV:MB photodegradation (a) pH and nanocatalyst and (b) dyes mixture and pH.

regarding the poor textural properties (low S_{BET} and V_P), the good photocatalytic activity of the nANA@CuO-NPs nanocatalyst can be justified by the reported E_g values.

In parallel, it is observable a blue shift is for CuO-NPs compared to nANA@CuO-NPs, in which the maximum reflectance changed from 720 nm for nANA@CuO-NPs to 570 nm for CuO-NPs, which agreed with the reports found in the literature for supported heterogeneous nanocatalysts [52]. Thus, it is expected that the sample nANA@CuO-NPs show higher light absorbance at $\lambda = 550\text{--}680$ nm, which is near to maximum light absorption of the dye molecules used in this study ($\lambda = 590$ nm for CV and $\lambda = 663$ nm for MB). Additionally, according to Table 5, the E_g for the supported nanocatalyst is lesser than the E_g for their counterparts evaluated from the Kubelka-Mung function and four Tauc plots, according to the literature [53]. Hence, the better photocatalytic activity of nANA@CuO-NPs than CuO-NPs is expected.

The thermal resistance of the samples is shown in Fig. 8, generated by TGA. CuO-NPs showed weight loss at 450 °C, whereas nANA no more

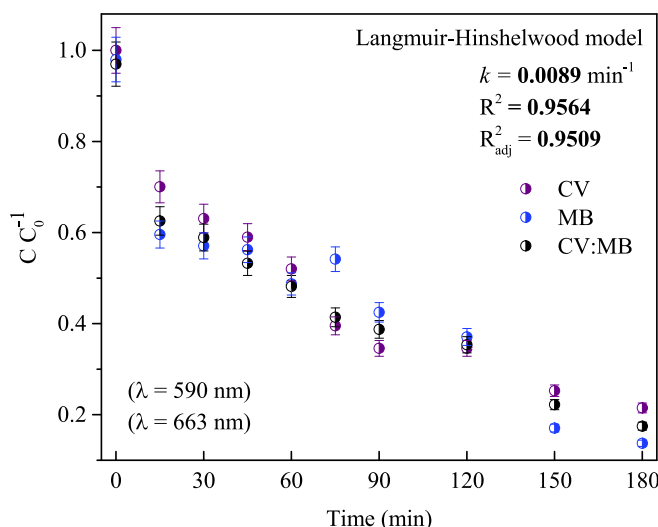


Fig. 12. Kinetic curve of photocatalytic degradation of the binary dye mixture. ($[\text{CV:MB}] = 135 \text{ mg/L}$ | $[\text{nANA@CuO-NPs}] = 1 \text{ g/L}$ | pH 7 | $25 \pm 2^\circ\text{C}$ | visible light radiation).

than 20 % of weight loss was observed, indicating that the nANA is more thermally stable than CuO-NPs. However, with the incorporation of the CuO-NPs into the nANA catalytic support, the thermal resistance tends to increase due to the synergic effect of the copper oxide nanoparticles and $[\text{AlO}_4]^{5-}$ and $[\text{SiO}_4]^{4-}$ present in the nANA@CuO-NPs structure. Thus, it was concluded that higher the thermal resistance of nANA@CuO-NPs was attributed to the presence of nANA in the nanocatalyst composition. For industrial purposes, the synthesized nanocatalyst can be considered a suitable alternative and resistant material for catalytic applications since the maximum temperature of the industrial wastewater commonly does not exceed 35°C . Noteworthy, the behavior of the CuO-NPs is attributed to the biogenic synthesis used to

prepare CuO, in which quercetin is present in the structure of the CuO-NPs. According to literature reports, quercetin shows about 40 % weight loss at 400°C , which is similar to the biogenic CuO-NPs thermal behavior, suggesting that the extract used for the biogenic synthesis was a quercetin-rich solution [53].

Fig. 9 shows the SEM-EDX results of the supported catalyst, catalytic support, and photoactive phase. According to Fig. 9(c) and 9(e), nANA and nANA@CuO-NPs resemble spherical morphology, whereas CuO-NPs (Fig. 9a) showed irregular shapes. Moreover, elementary composition by EDX (Fig. 9b, 9d, and 9f) reported for the nANA@CuO-NPs: Cu (32.21 wt%), O (40.94 wt%), C (10.23 wt%), Si (6.83 wt%), Al (4.86 wt %) and Na (4.81 wt%), denoting Si/Al ratio < 2 (1.36), classifying nANA as a low silica nanozeolite [54].

3.2. Characterization of the *Camellia sinensis* extract

Table 6 shows the determination of flavonoids and total phenols, where the *Camellia sinensis* extract showed high content of flavonoids and total phenols.

As can be seen in Table 6, it was reported about 18 mg g^{-1} of flavonoids and total phenols in the chemical composition of the *Camellia sinensis* extract, suggesting a high reducing ability of the green tea. Furthermore, considering the TGA studies mentioned before, there was indicative of the presence of quercetin in the extract as the main reducing agent of the biogenic synthesis of CuO-NPs, once it partially degrades (40 % weight loss) at a temperature near 500°C .

3.3. CCRD 2³

The ideal condition of the photocatalytic degradation of the dye mixture was evaluated by CCRD 2. Thus, Tables 7 and 8 show the observed values of degradation percent and the metrics of the model developed from the CCRD 2³, respectively.

According to Table 7, the experimental set number 9 was identified as the ideal condition provided by CCRD at pH = 7, $[\text{CV:MB}] = 135 \text{ mg/L}$, and $[\text{nANA@CuO-NPs}] = 1 \text{ g/L}$ with 82.24 % for the CV:MB

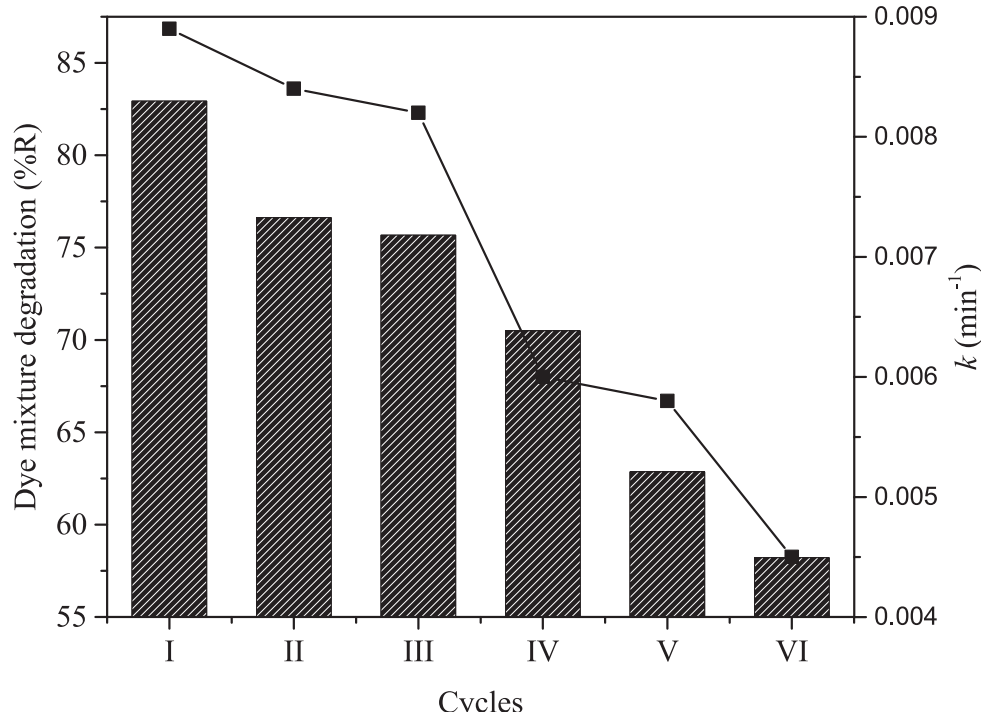


Fig. 13. Effect of the reuse of nANA@CuO-NPs in heterogeneous photocatalytic process. ($[\text{CV:MB}] = 135 \text{ mg/L}$ | $[\text{nANA@CuO-NPs}] = 1 \text{ g/L}$ | pH 7 | $25 \pm 2^\circ\text{C}$ | visible light radiation).

Table 9
ML algorithm performances and best configuration.

Algorithm	Training R ²	Training RMSE	Testing R ²	Testing RMSE	Best algorithm configuration
DT	0.7044	5.9383	0.6121	6.6500	Number of decision trees: 50 max. tree depth: 15 m
RF	0.6990	5.9571	0.4905	7.0235	Number of decision trees: 50 Max. tree depth: 5 m Sampling: bootstrap sampling
XGB	0.8103	5.0857	0.9880	2.3605	Booster method: dart Max. tree depth: 6 m Initial learning rate: 0.10 (~10 %)
ANN	0.75794	52.1349	0.6152	73.3946	Number of epochs: 90,000 Activation function: hyperbolic tangent function Weight updating function: lbfgs Neural network: 6-12-1* Initial learning rate: 0.1 (~10 %)

*1 hidden layer with 12 neurons.

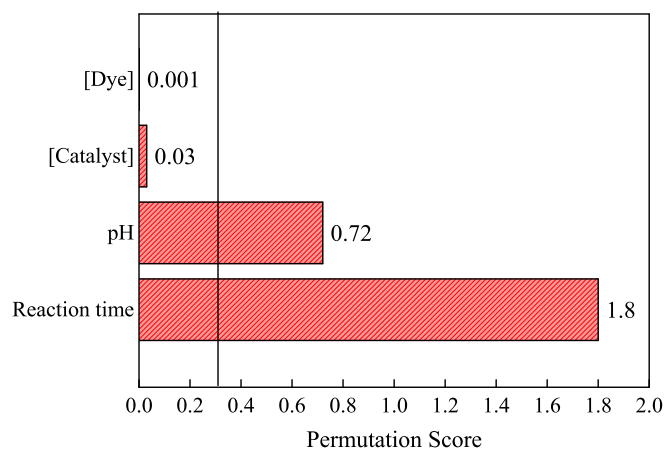


Fig. 14. Influence of each parameter on the *m/z* prediction.

photodegradation. Table 8 shows the ANOVA analysis of variance to %R photodegradation, where it was possible to verify that the model was predicted due to the F_{CAL} (19.3) was 5 times greater than the F_{TAB} (3.68), where 94.72 % of the experimental values were adjusted to the model. The Pareto chart is presented in Fig. 10, in which the influence of each parameter is addressed.

Eq. (15) shows the effect of nanocatalyst concentration and pH, whereas Eq. (16) considers the effect of pH and dye mixture concentration in the response. According to Eq. (15), the dye mixture

degradation (%R) showed a linear and quadratic dependency of the nanocatalyst concentration and pH, indicating that a minor change in these variables can generate so different response. Moreover, it suggests that there is a minimum/maximum value expected for pH and [nANA@CuO-NPs] to achieve the highest dye removal, with the values toward them too low or too high. The same behavior is observed in Eq. (16) for pH and [CV:MB].

$$\%R = 78.9 + 45.6 * [\text{nANA@CuO - NPs}] - 11.4 * [\text{nANA@CuO - NPs}]^2 + 7.8 * \text{pH} - 0.94 * \text{pH}^2 + 0.26 * \text{pH} * [\text{nANA@CuO - NPs}] \quad (15)$$

$$\%R = -25.34 + 0.83 * \text{pH} - 0.003 * \text{pH}^2 + 7.84 * [\text{CV:MB}] - 0.93 * [\text{CV:MB}]^2 - 0.20 * [\text{CV:MB}] + 0.03 * [\text{CV:MB}] * \text{pH} + 0.26 * \text{pH} + 36.18 \quad (16)$$

Fig. 11 shows the surface response generated from CCRD 2³ is shown.

According to Fig. 11(a) and 11(b), at neutral, pH higher and %R values were achieved, at [nANA@CuO-NPs] near 1.0 g L⁻¹ and [CV:MB] ranged from 90 to 140 mg/L.

3.4. Kinetic of degradation

The kinetic of degradation of the dye mixture is presented in Fig. 12.

According to Fig. 12, about 80–86 % degradation was reported for the CV:MB binary dye mixture. Moreover, the molar composition of the binary dye mixture measured was 0.44 % (by mole) of CV and 0.56 % MB, which is remarkably close to the equimolar composition proposed in this work. Higher removal was achieved for MB (86.25 %) than CV (78.49 %) in practice, which is attributed to the smaller molecular volume of MB than CV dye. In addition, MB can be more easily adsorbed onto the nANA@CuO-NPs surface, which explains these results. Moreover, the molar mass of MB dye (319.85 g mol⁻¹) is smaller than CV dye (407.979 g mol⁻¹), being able to penetrate more easily inside the nanocatalyst pores.

In parallel, the cationic nature of the organic dyes seems to boost the degradation, once they tend to repel each other in solution, occasioning the transferring of the smaller dye molecule (MB) to the surface of the nanocatalyst and hence, more degradation.

Furthermore, Langmuir-Hinshelwood represented a good fit of experimental data, since R² and R_{adj}² were slightly close to unity. Moreover, the apparent rate of the pseudo first-order reaction (*k*) evaluated for the binary dye mixture was 0.0089 min⁻¹, suggesting that about 0.89 % of the dye molecules are degraded at each minute of the heterogeneous photocatalysis [55]. Thereafter, it is expected that about 80.10 % of the dye molecules are degraded after 90 min, which is remarkably close to values observed at the end of treatment. However, this value (~80 % dye mixture degradation) is achieved in shorter times (after 180 min) probably due to electron-hole pair recombination and side reactions (e.g., isomerization) that take place during the process [56].

Based on the low Eg, wide light absorption, and the internal electrical field created by the zeolite in the nANA@CuO-NPs, is expected a S-scheme for this supported nanocatalyst. Additionally, the high degradation percentage of the dye mixture can be attributed to the low recombination rate of the catalyst (then low heat loss during the process) resulting from this arrangement (S-scheme of nANA@CuO-NPs), providing higher generation of O₂[·] and HO[·] in the aqueous media [57]. In S-scheme, useful photogenerated electrons and holes move in opposite directions, while useless photogenerated electrons/holes recombine due to electrostatic forces without affecting the redox reactions in the photocatalytic process [58]. Moreover, the negative charge of zeolite and the ability of copper to lose electrons strengthen this assumption.

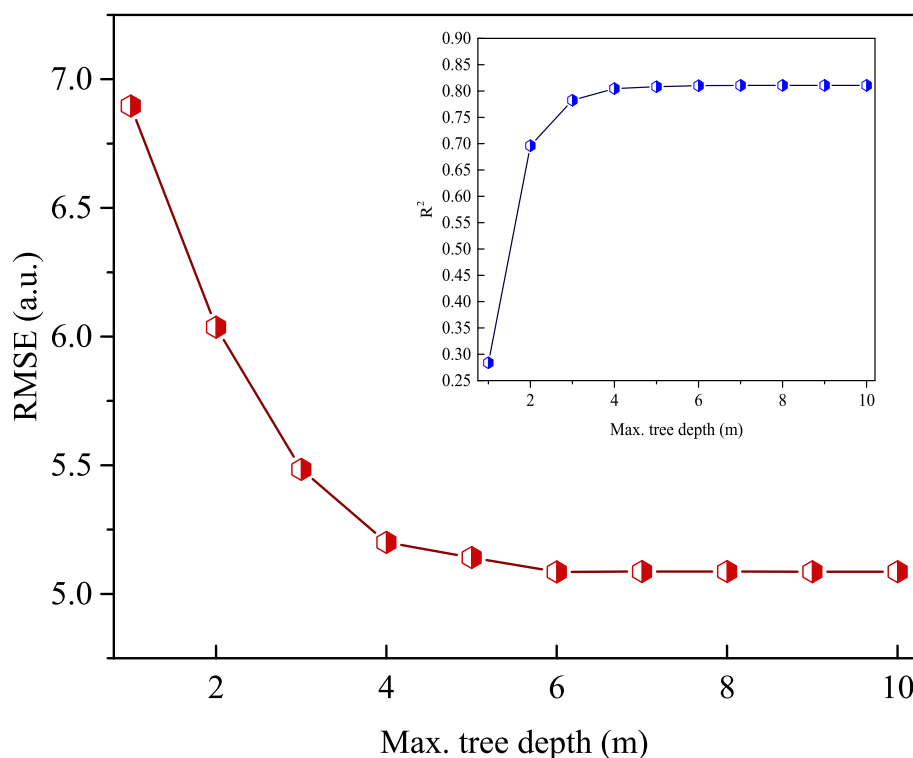


Fig. 15. Effect of the maximum tree depth on the algorithm performance (training dataset).

3.5. Reuse of the supported nanocatalyst

Fig. 13 shows the results found for the reuse study of the synthesized nanocatalyst, under visible light and ideal conditions determined from CCRD 2³.

According to Fig. 13, despite the high photocatalytic activity of the nANA@CuO-NPs in the CV:MB dye mixture degradation, an expressive decrease of rate constant and degradation percentage was observed after the four cycles of heterogeneous photocatalysis. It is probably because of some active sites of the nanocatalyst being occupied by adsorbed water and dye molecules, thus reduction photocatalytic activity after the V cycle (lesser amount of active sites of the nANA@CuO-NPs available for dye molecules). Hence, it is suggested washing and drying steps before reintroducing the nanocatalyst back to the photocatalytic reactor as an alternative to overcome this drawback.

A similar tendency was found in the literature reports, where a dye mixture consisting of CV and MO dyes was degraded under visible irradiation (first cycle: 85.95 %), resulting in a decrease of 9 % and 11 % observed for the second and third cycles, in which no washing and drying step was carried out [59]. Nevertheless, the second and third cycles showed similar values for %R (78.27 % and 76.41 %) and k (0.0084 min⁻¹ and 0.082 min⁻¹), which is considered interesting from an industrial viewpoint.

3.6. Degradation pathway elucidation

The dataset used (collected from articles involving photocatalytic degradation of MB and CV dyes under visible light, with the degradation products identified by GC-MS) in the machine learning study was arranged in a matrix form constituted of 90 rows and 5 columns. The data were coded and compiled in Python 3.8 version open-source (Google Colaboratory) with the importation of keras, tensorflow and scikit-learn libraries. Thereafter, Table 9 informs the model performance of each algorithm tested in the machine learning study for degradation pathway elucidation.

According to Table 9, the ANN was less adequate for predicting the

dye mixture degradation pathway of high errors (RMSE ranged from ~52 to ~73 for *m/z* prediction) generated from this algorithm. Nevertheless, DT and RF can be selected as baseline algorithms to develop the regression model for *m/z* estimation, once the RMSEs for training and testing datasets are closed. Despite the low values of RMSE in these models, the XGB was selected as the more adequate algorithm for *m/z* prediction and hence dye binary mixture degradation products due to the lower RMSE (5.086 for training and 2.360 for testing dataset) associated with XGB data prediction and higher R² (0.810 and 0.988) values than the other algorithms. In addition, RMSE_{testing} < RMSE_{training} and R²_{testing} > R²_{training} suggests that XGB showed satisfactory performance in predicting new data to the model. To the best of our knowledge, Fig. 14 informs the feature importance study, measured by the permutation score for each input parameter, generated from the XGB model.

The permutation score obeys the Pareto statement, in which 80 % of the observed results can be explained by 20 % of the input data. Thus, according to Fig. 14, the parameters pH and reaction time strongly influenced the response of the proposed model, *m/z*. The greater the permutation scores greater the influence of the feature (input variable) on the response. Catalyst and dye concentration showed to not be important in the reaction pathway of the MB degradation. However, depending on the reaction time, specific species are generated as intermediate or (by)products. According to experimental results, the higher the time higher the amount of low-mass chemical species observed [60]. Moreover, Fig. 13 also suggests that alterations in pH can significantly affect the intermediates and products formed during the degradation reaction, which was confirmed in experimental runs found in the literature [61]. Fig. 15 demonstrates the effect of the maximum tree depth on the machine learning-based model performance.

According to Fig. 15, the maximum tree depth of 6 m resulted in the lowest RMSE (RMSE_{training} ~ 5.20), achieving a *plateau* at max. tree depth 7 m. Moreover, the inset of Fig. 12 shows a similar behavior, revealing that high R²_{training} (~0.81) is achieved at 6 m. Thus, 6 m was used as the maximum tree depth in the testing dataset. At the final run of XGB for the testing dataset, it was observable that R₂ increased to 0.9880

Dataset: data collected from scientific papers involving photocatalytic degradation of CV and MB dyes, in which the main degradation products were identified by CG-MS

4 inputs: time | dye concentration | catalyst concentration | pH

1 output: m/z ratio, associated to molar mass

Data size: 90 data points (normalized in values ranging from 0 to 1)

Machine Learning algorithm: Xtreme Gradient Boosting Machine (XGB) |

XGB parameters: Booster method: dart | max. tree depth: 6 m | Initial learning rate: 0.10 (~10%)

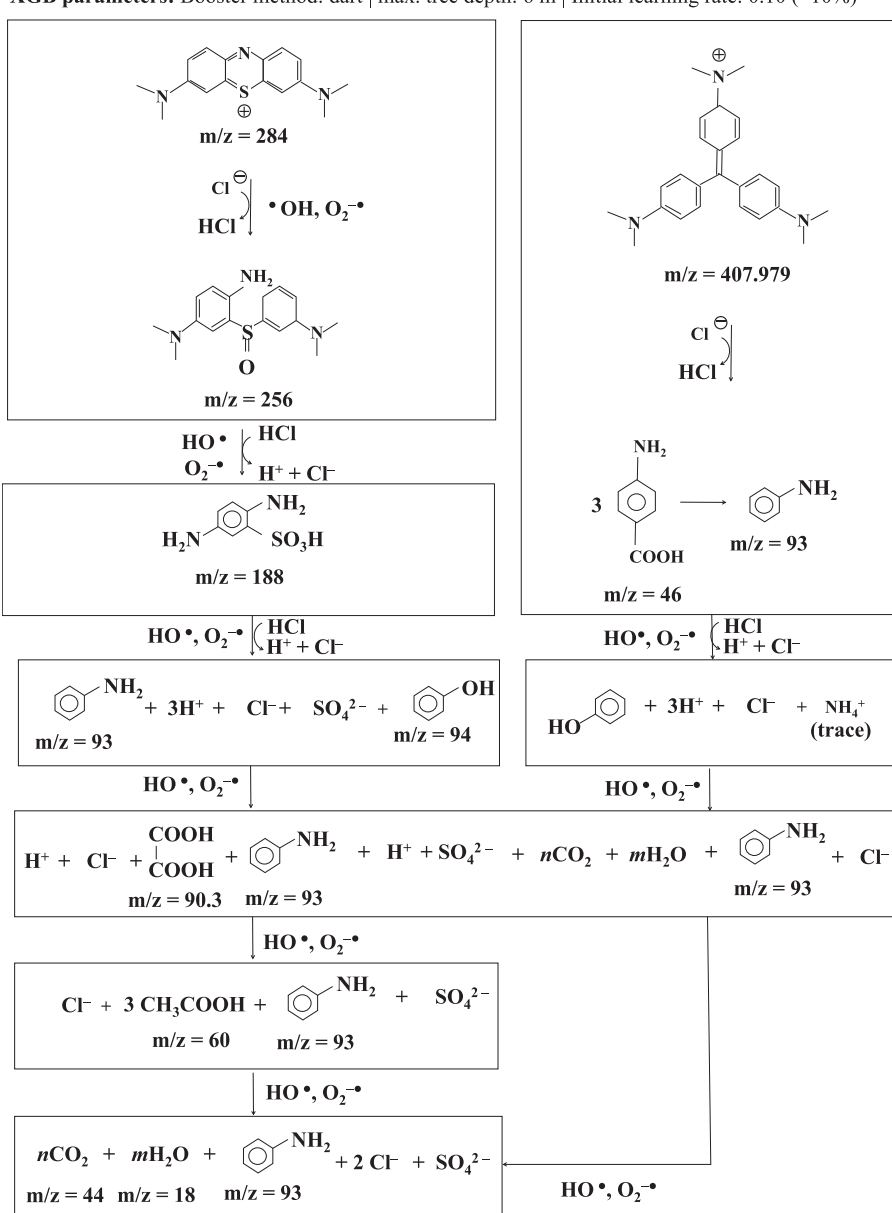


Fig. 16. General reaction pathway for CV:MB degradation under visible light.

and RMSE reduced to 2.3605.

Fig. 16 illustrates the generalized reaction pathway proposed for CV and MB dye degradation observed for the experimental procedure of this work.

According to Fig. 16, the final products of the photocatalytic degradation of CV ($m/z = 409.797$) and MB ($m/z = 284$) dye mixture were carbon dioxide (CO_2 , $m/z = 44$), water (H_2O , $m/z = 18$), aniline ($\text{C}_6\text{H}_5\text{NH}_2$, $m/z = 93$), sulfide (SO_4^{2-}) and chloride ions (Cl^-), respectively. The degradation of the binary dye mixture achieved was 82.84 %, suggesting that the remaining (23.07 %) corresponded to unreacted CV and MB dyes. Another explanation can be attributed to the formation of internal interactions of MB or CV monomers, generating dimmers and trimers [62]. Dimmers of MB were reported to resist degradation, with

light absorption at 565 and 606 nm, which are degraded gradually. However, the presence of monomers, dimmers and trimmer of CV can result in electrostatic repulsion between MB dye molecules, thus reducing the formation of resistant dimmers, which increase the photocatalytic degradation of dyes.

It is worth pointing out that the presence of aniline in the aqueous solution and the amount of chloride and sulfate ions should be analyzed to check the water quality. These ions are naturally found in surface water and wastewater composition, being not damaging to humans and aquatic life dependent on their concentration. Moreover, the proposed photocatalytic process was considered promising, once crystal violet and methylene blue dyes are converted to low-mass and less toxic compounds (CO_2 , H_2O , SO_4^{2-} , Cl^-) and aniline, which can be easily removed

from water by the next cycle of heterogeneous photocatalysis or by adsorption onto a low-cost nanoadsorbent (e.g., nanozeolites synthesized from agro-industrial waste).

4. Conclusion

In this work, the synthesis of a novel supported heterogeneous nanocatalyst (nANA@CuO-NPs) and its use in the degradation of a binary dye mixture was proposed. The crystallite diameter, particle size, and FEG-SEM results confirmed that all samples (supported catalyst, catalytic support, and photoactive phase) are on a nanometric scale, being classified as nanomaterials. Thus, CuO-NPs from biogenic synthesis and nANA form (agro)industrial waste was successfully prepared. Moreover, as identified by XRD, high-purity nanomaterials were obtained by the proposed methods, in which tenorite and analcime phases were found for CuO-NPs and nANA, respectively. Regarding ATR-FTIR, typical functional groups of CuO-NPs and nANA in the sample nANA@CuO-NPs were identified, confirming the success of the impregnation method. Regarding textural properties, the surface of CuO-NPs has increased from $2\text{ m}^2/\text{g}$ to $15\text{ m}^2/\text{g}$, whereas pore diameter and pore volume reduced from 37 to 15 nm and from 0.046 to 0.0037 $\text{cm}^3\text{ g}^{-1}$, respectively. Furthermore, nANA@CuO-NPs resulted in better thermal resistance, which was attributed to the presence of the nANA in its chemical composition. Moreover, SEM-EDX results showed that the nANA showed Si/Al < 2 (being classified as low-silica nanozeolite) and the chemical composition for nANA@CuO-NPs was C (43.72 %), O (43.37 %), Si (5.44 %), Al (3.99 %) Na (2.99 %) and Cu (0.49 %), respectively. The prepared nanocatalyst showed physio-chemical stability due to the electrostatic interactions, reduced band gap energy ($E_g = 1.67\text{ eV}$) compared to the CuO-NPs ($E_g = 2.22\text{ eV}$), which improved photocatalytic activity of the nANA@CuO-NPs. Moreover, CCDR 2³ indicated a good predictive ability, where the $F_{\text{calculated}}$ (19.3) was greater than the $F_{\text{tabulated}}$ (3.68). The model informed that pH, nanocatalyst, and dye binary mixture concentration affects linearly and quadratically the degradation percent (%R). Additionally, ML-based algorithms for the elucidation of the reaction degradation pathway, in which four machine learning algorithms were used. The algorithm XGB showed the best performance ($R_{\text{training}}^2 = 0.8103$, $R_{\text{testing}}^2 = 0.9880$, RMSE_{training} = 5.0857 RMSE_{testing} = 2.3605) in the prediction of the main degradation products based on GC-MS data for the CV and MB photodegradation. The higher R^2 for the testing dataset suggested that the developed model was suitable for the prediction of new data (m/z from pH, reaction time, nanocatalyst, and organic dye concentrations). The importance study revealed that the pH and the reaction time were the variables that most affect the response variable estimation, m/z . The catalyst reuse study revealed the stability of the nANA@CuO-NPs after VI cycles of the heterogeneous photocatalysis, suggesting that the drying step should be carried out to remove adsorbed molecules on the nanomaterial. Therefore, the use of plant extracts and industrial solid residues as suitable precursors of the synthesis of copper oxide nanostructures and nanozeolite was confirmed, generating an alternative nanocatalyst with good potentiality for binary dye mixture by heterogeneous photocatalyst.

CRediT authorship contribution statement

Leandro Rodrigues Oviedo: Writing – review & editing, Writing – original draft, Validation, Investigation, Formal analysis, Data curation, Conceptualization. **Daniel Moro Durzian:** Writing – review & editing, Writing – original draft, Formal analysis, Data curation. **Giane Engel Montagner:** Writing – review & editing, Writing – original draft, Formal analysis, Data curation. **Yolice Patricia Moreno Ruiz:** Writing – review & editing, Formal analysis. **André Galembeck:** Writing – review & editing, Formal analysis. **Giovani Pavoski:** Writing – review & editing, Formal analysis. **Denise Crocce Romano Espinosa:** Writing – review & editing, Formal analysis. **Lissandro Dorneles Dalla Nora:** Writing –

review & editing, Formal analysis. **William Leonardo da Silva:** Writing – review & editing, Writing – original draft, Validation, Supervision, Project administration, Methodology, Investigation, Formal analysis, Data curation, Conceptualization.

Declaration of competing interest

The authors declare that they have no known competing financial interests or personal relationships that could have appeared to influence the work reported in this paper.

Data availability

Data will be made available on request.

Acknowledgments

Authors would also like to thank Department of Fundamental Chemistry (DQF), LAREX (USP, Brazil-SP) and Franciscan University for instrumental support. This study was financed by the CAPES (Coordination of Superior Level Staff Improvement) - Finance Code 001.

References

- [1] H.R. Dihom, M.M. Al-Shabani, R.M.S.R. Mohamed, A.A. Al-Gheethi, A. Sharma, M. H.B. Khamidun, Photocatalytic degradation of disperse azo dyes in textile wastewater using green zinc oxide nanoparticles synthesized in plant extract: A critical review, *J. Water Process Eng.* 47 (2022) 47102705–47102716, <https://doi.org/10.1016/j.jwpe.2022.102705>.
- [2] R. Kishor, D. Purchase, G.D. Saratale, R.G. Saratale, L.F.R. Ferreira, M. Bilal, R. Chandra, R.N. Bharagava, Ecotoxicological and health concerns of persistent coloring pollutants from textile industry wastewater and treatment approaches for environmental safety, *J. Environ. Chem. Eng.* 9 (2021) 105012–105029, <https://doi.org/10.1016/j.jece.2020.105012>.
- [3] M.A. Ahmed, Z.M. Abou-Gamra, H.A.A. Medien, M.A. Hamza, Effect of porphyrin on photocatalytic activity of TiO₂ nanoparticles toward Rhodamine B photodegradation, *J. Photochem. Photobiol. B Biol.* 176 (2017) 25–35, <https://doi.org/10.1016/j.jphotobiol.2017.09.016>.
- [4] C. Hou, B. Hu, J. Zhu, Photocatalytic degradation of methylene blue over TiO₂ pretreated with varying concentrations of NaOH, *Catalysts* 8 (2018) 575–587, <https://doi.org/10.3390/catal8120575>.
- [5] A. Nezamzadeh-Ejhieh, Z. Banan, A comparison between the efficiency of CdS nanoparticles/zeolite A and CdO/zeolite A as catalysts in photodecolorization of crystal violet, *Desalination* 279 (2011) 146–151, <https://doi.org/10.1016/j.desal.2011.06.006>.
- [6] A. Nezamzadeh-Ejhieh, Z. Banan, Sunlight assisted photodecolorization of crystal violet catalyzed by CdS nanoparticles embedded on zeolite A, *Desalination* 284 (2012) 157–166, <https://doi.org/10.1016/j.desal.2011.08.050>.
- [7] S.A. Mirsalari, A. Nezamzadeh-Ejhieh, A.R. Massah, A designed experiment for CdS-AgBr photocatalyst toward methylene blue, *Environ. Sci. Pollut. Res.* 29 (2022) 33013–33032, <https://doi.org/10.1007/s11356-021-17569-1>.
- [8] W. Zhao, Y. Liu, Z. Wei, S. Yang, H. He, S. Sun, Fabrication of a novel p-n heterojunction photocatalyst n-BiVO₄@p-MoS₂ with core-shell structure and its excellent visible-light photocatalytic reduction and oxidation activities, *Appl. Catal. B Environ.* 185 (2016) 242–252, <https://doi.org/10.1016/j.apcatb.2015.12.023>.
- [9] D. Olivo-Alanís, A. García-González, M.A. Mueses, R.B. García-Reyes, Generalized kinetic model for the photocatalytic degradation processes: Validation for dye wastewater treatment in a visible-LED tubular reactor, *Appl. Catal. B Environ.* 317 (2022) 121804–121815, <https://doi.org/10.1016/j.apcatb.2022.121804>.
- [10] P. Mohammadyari, A. Nezamzadeh-Ejhieh, Supporting of mixed ZnS–NiS semiconductors onto clinoptilolite nano-particles to improve its activity in photodegradation of 2-nitrotoluene, *RSC Adv.* 5 (2015) 75300–75310, <https://doi.org/10.1039/c5ra12608h>.
- [11] O.B. Macedo, A.L.M. de Oliveira, I.M.G. dos Santos, Zinc tungstate: a review on its application as heterogeneous photocatalyst, *Cerâmica* 68 (2022) 294–315, <https://doi.org/10.1590/0366-69132022683873265>.
- [12] A. Yousefi, A. Nezamzadeh-Ejhieh, Preparation and characterization of SnO₂-BiVO₄-CuO catalyst and kinetics of phenazopyridine photodegradation, *Iran. J. Catal.* 11 (2021) 247–259.
- [13] M. Rezaei, A. Nezamzadeh-Ejhieh, A.R. Massah, A comprehensive review on the boosted effects of anion vacancy in the heterogeneous photocatalytic degradation, part I: Focus on sulfur, nitrogen, carbon, and halogen vacancies, *Ecotoxicol. Environ. Saf.* 269 (2024) 115927, <https://doi.org/10.1016/j.ecoenv.2024.115927>.
- [14] F. Sanakousar, C.C. Vidyasagar, S.S. Chigari, V.M. Jiménez-Pérez, C.C. Viswanath, P. Karoyajananvar, M.B. Sridhara, Effect of surfactant on structural and optical properties of V₂O₅ nanocrystals as a potential catalyst for photodegradation, *Iran. J. Catal.* 13 (2023) 57–72. 10.30495/ijc.2023.1973011.1975.

- [15] F. Iazdani, A. Nezamzadeh-Ejhieh, Photocatalytic kinetics of 2,4-dichloroaniline degradation by NiO-clinoptilolite nanoparticles, *Spectrochim. Acta - Mol. Biomol. Spectrosc.* 250 (2021) 119228–119237, <https://doi.org/10.1016/j.saa.2020.119228>.
- [16] F.R. Praxedes, M.A.L. Nobre, P.S. Poon, J. Matos, S. Lanfredi, Nanostructured KxNa(1-x)NbO₃ hollow spheres as potential materials for the photocatalytic treatment of polluted water, *Appl. Catal. B Environ.* 298 (2021) 120502–120521, <https://doi.org/10.1016/j.apcatb.2021.120502>.
- [17] J. Zhang, J. Liang, H. Peng, H. Mi, P. Luo, H. Xu, M. He, P. Wu, Cost-effective fast-synthesis of chabazite zeolites for the reduction of NO_x, *Appl. Catal. B Environ.* 292 (2021) 120163–120174, <https://doi.org/10.1016/j.apcatb.2021.120163>.
- [18] F. Soori, A. Nezamzadeh-Ejhieh, Synergistic effects of copper oxide-zeolite nanoparticles composite on photocatalytic degradation of 2,6-dimethylphenol aqueous solution, *J. Mol. Liq.* 255 (2018) 250–256, <https://doi.org/10.1016/j.molliq.2018.01.169>.
- [19] Z. Amani-Beni, A. Nezamzadeh-Ejhieh, Construction of a sensitive non-enzymatic fructose carbon paste electrode – CuO nanoflower: designing the experiments by response surface methodology, *New J. Chem.* 42 (2018) 1021–1030, <https://doi.org/10.1039/C7nj03124f>.
- [20] A. Nezamzadeh-Ejhieh, M. Karimi-Shamsabadi, Decolorization of a binary azo dyes mixture using CuO incorporated nanozeolite-X as a heterogeneous catalyst and solar irradiation, *Chem. Eng. J.* 228 (2013) 631–641, <https://doi.org/10.1016/j.cej.2013.05.035>.
- [21] K. Ganeshan, V.K. Jothi, A. Natarajan, A. Rajaram, R. Siranjeevi, S. Ramalingam, Green synthesis of copper oxide nanoparticles decorated with graphene oxide for anticancer activity and catalytic applications, *Arab. J. Chem.* 13 (2020) 6802–6814, <https://doi.org/10.1016/j.arabjc.2020.06.033>.
- [22] Anju, S. Sharma, H.R. Dhanetia, A. Sharma, Green synthesis of copper nanoparticles using *Holopeltis integrifolia* fruit extract, *Rasayan J. Chem.* 13 (2020) 2664–2671. 10.31788/rjc.2020.1346306.
- [23] M. Bahramian, R.K. Dereli, W. Zhao, M. Giberti, E. Casey, Data to intelligence: The role of data-driven models in wastewater treatment, *Expert Syst. Appl.* 217 (2023) 119453–119472, <https://doi.org/10.1016/j.eswa.2022.119453>.
- [24] S. Athavale, D.P. Barai, B.A. Bhanvase, S.L. Pandharipande, Investigation on performance of Eu:GO:KSrPO₄ nanocomposite for MB dye photocatalytic degradation: Experimental and ANN modeling, *Optik (stuttgart)* 275 (2023) 170561–170579, <https://doi.org/10.1016/j.jileo.2023.170561>.
- [25] M. Liu, W. Li, Prediction and analysis of corrosion rate of 3C steel using interpretable machine learning methods, *Mater. Today Commun.* 35 (2023) 106408–106417, <https://doi.org/10.1016/j.mtcomm.2023.106408>.
- [26] L.R. Oviedo, P.C.L. Muraro, G. Pavoski, D.C.R. Espinosa, Y.P.M. Ruiz, A. Galembek, C.R.B. Rhoden, W.L. Da Silva, Synthesis and characterization of nanozeolite from (agro)industrial waste for application in heterogeneous photocatalysis, *Environ. Sci. Pollut. Res.* 29 (2022) 3794–3807, <https://doi.org/10.1007/s11356-021-15815-0>.
- [27] J.E. Jeronisa, L.A. Joseph, P.A. Vinosa, A.J. Mary, S.J. Das, Camellia Sinensis leaf extract mediated synthesis of copper oxide nanostructures for potential biomedical applications, *Mater. Today Proc.* 8 (2019) 214–222, <https://doi.org/10.1016/j.mtproc.2019.02.103>.
- [28] A. Nezamzadeh-Ejhieh, S. Hushmandrad, Solar photodecolorization of methylene blue by CuO/X zeolite as a heterogeneous catalyst, *Appl. Catal. A Gen.* 388 (2010) 149–159, <https://doi.org/10.1016/j.apcata.2010.08.042>.
- [29] A. Stavrinou, C.A. Aggelopoulos, C.D. Tsakiroglou, Exploring the adsorption mechanisms of cationic and anionic dyes onto agricultural waste peels of banana, cucumber and potato: Adsorption kinetics and equilibrium isotherms as a tool, *J. Environ. Chem. Eng.* 6 (2018) 6958–6970, <https://doi.org/10.1016/j.jece.2018.10.063>.
- [30] M. Farsi, A. Nezamzadeh-Ejhieh, A Z-scheme Cobalt(II) oxide-silver tungstate nano photocatalyst: Experimental design and mechanism study for the degradation of methylene blue, *Surf. Interf.* 32 (2022) 102148, <https://doi.org/10.1016/j.surfin.2022.102148>.
- [31] S. Ghattavi, A. Nezamzadeh-Ejhieh, GC-MASS detection of methyl orange degradation intermediates by AgBr/g-C3N4: Experimental design, bandgap study, and characterization of the catalyst, *Inter. J. Hydrogen Energy.* 45 (2020) 24636–24656, <https://doi.org/10.1016/j.ijhydene.2020.06.207>.
- [32] N. Mehrabpour, A. Nezamzadeh-Ejhieh, S. Ghattavi, A. Ershadi, A magnetically separable clinoptilolite supported CdS-PbS photocatalyst: Characterization and photocatalytic activity toward cefotaxime, *Appl. Surf. Sci.* 614 (2023) 156252, <https://doi.org/10.1016/j.apusc.2022.156252>.
- [33] D. Kumar, N. Verma, C.B. Singh, A.K. Singh, Crystallite size strain analysis of nanocrystalline La_{0.7}Sr_{0.3}MnO₃ perovskite by Williamson-Hall plot method, *AIP Conference Proceedings* 1942 (2018), <https://doi.org/10.1063/1.5028655>.
- [34] R. Roesler, L.G. Malta, L.C. Carrasco, R.B. Holanda, C.A.S. Sousa, G.M. Pastore, Antioxidant activity of cerrado fruits, *Food Sci. Technol.* 27 (2007) 53–60, <https://doi.org/10.1590/S0101-20612007000100010>.
- [35] J. Zhishen, T. Mengcheng, W. Jianming, The determination of flavonoid contents in mulberry and their scavenging effects on superoxide radicals, *Food Chem.* 64 (1999) 555–559, [https://doi.org/10.1016/S0308-8146\(98\)00102-2](https://doi.org/10.1016/S0308-8146(98)00102-2).
- [36] D.A. Yaseen, M. Scholz, Textile dye wastewater characteristics and constituents of synthetic effluents: a critical review, *Int. J. Environ. Sci. Technol.* 16 (2019) 1193–1226, <https://doi.org/10.1007/s13762-018-2130-z>.
- [37] N.G. Asenjo, R. Santamaría, C. Blanco, M. Granda, P. Álvarez, R. Menéndez, Correct use of the Langmuir-Hinshelwood equation for proving the absence of a synergy effect in the photocatalytic degradation of phenol on a suspended mixture of titania and activated carbon, *Carbon* 55 (2013) 62–69, <https://doi.org/10.1016/j.carbon.2012.12.010>.
- [38] Z.H. Jaffari, A. Abbas, S.M. Lam, S. Park, K. Chon, E.S. Kim, K.H. Cho, Machine learning approaches to predict the photocatalytic performance of bismuth ferrite-based materials in the removal of malachite green, *J. Hazard. Mater.* 442 (2023) 130031–130042, <https://doi.org/10.1016/j.jhazmat.2022.130031>.
- [39] A. El Bey, M. Laidi, A. Yetto, S. Hanini, A. Ibrir, M. Bentabli, H. Ouldkaoua, Practical Artificial Neural Network Tool for Predicting the Competitive Adsorption of Dyes on Gemini Polymeric Nanoarchitecture, *Kem. Ind.* 70 (2021) 481–488. 10.15255/kui.2020.069.
- [40] X. Yuan, M. Suvarna, S. Low, P.D. Dissanayake, K.B. Lee, J. Li, X. Wang, Y.S. Ok, Applied machine learning for prediction of CO₂ adsorption on biomass waste-derived porous carbons, *Environ. Sci. Technol.* 55 (2021) 11925–11936, <https://doi.org/10.1021/acs.est.1c01849>.
- [41] S. Vahabirad, A. Nezamzadeh-Ejhieh, Co-precipitation synthesis of BiOI/(BiO)2CO₃: Brief characterization and the kinetic study in the photodegradation and mineralization of sulfasalazine, *J. Solid State Chem.* 310 (2022) 123018–123025, <https://doi.org/10.1016/j.jssc.2022.123018>.
- [42] S. Senobar, A. Nezamzadeh-Ejhieh, A comprehensive study on the enhanced photocatalytic activity of CuO-NiO nanoparticles: Designing the experiments, *J. Mol. Liq.* 261 (2018) 208–217, <https://doi.org/10.1016/j.molliq.2018.04.028>.
- [43] M. Karimi-Shamsabadi, A. Nezamzadeh-Ejhieh, Comparative study on the increased photoactivity of coupled and supported manganese-silver oxides onto a natural zeolite nanoparticles, *J. Mol. Catal. A Chem.* 418–419 (2016) 103–114, <https://doi.org/10.1016/j.molcata.2016.03.034>.
- [44] H.S. Hashemi, A. Nezamzadeh-Ejhieh, M. Karimi-Shamsabadi, A novel cysteine sensor based on modification of carbon paste electrode by Fe(II)-exchanged zeolite X nanoparticles, *Mater. Sci. Eng. c* 58 (2016) 286–293, <https://doi.org/10.1016/j.msec.2015.08.051>.
- [45] L. Ahmadpour-Mobarakeh, A. Nezamzadeh-Ejhieh, A zeolite modified carbon paste electrode as useful sensor for voltammetric determination of acetaminophen, *Mater. Sci. Eng. C* 49 (2015) 493–499, <https://doi.org/10.1016/j.msec.2015.01.028>.
- [46] L.J. Garces, V.D. Makwana, B. Hincapie, A. Sacco, S.L. Suib, Selective N, N-methylation of aniline over cocrystallized zeolites RHO and zeolite X (FAU) and over Linde type L (Sr, K-LTL), *J. Catal.* 217 (2003) 107–116, [https://doi.org/10.1016/S0021-9517\(03\)00048-4](https://doi.org/10.1016/S0021-9517(03)00048-4).
- [47] M. Thommes, K. Kaneko, A.V. Neimark, J.P. Olivier, F. Rodriguez-Reinoso, J. Rouquerol, K.S.W. Sing, Physisorption of gases, with special reference to the evaluation of surface area and pore size distribution (IUPAC Technical Report), *Pure Appl. Chem.* 87 (2015) 1051–1069, <https://doi.org/10.1515/pac-2014-1117>.
- [48] D.L. Postai, C.A. Demarchi, F. Zamatta, D.C.C. Melo, C.A. Rodrigues, Adsorption of rhodamine B and methylene blue dyes using waste of seeds of *Aleurites Moluccana*, a low cost adsorbent, *Alexandria Eng. J.* 55 (2016) 1713–1723, <https://doi.org/10.1016/j.aej.2016.03.017>.
- [49] S. Mohammadnejad, J.L. Provis, J.S.J. Van Deventer, Gold sorption by silicates in acidic and alkaline chloride media, *Int. J. Miner. Process.* 100 (2011) 149–156, <https://doi.org/10.1016/j.minpro.2011.05.013>.
- [50] S. Fasolin, M. Romano, S. Boldrini, A. Ferrario, M. Fabrizio, L. Armelao, S. Barison, Single-step process to produce alumina supported hydroxy-sodalite zeolite membranes, *J. Mater. Sci.* 54 (2019) 2049–2058, <https://doi.org/10.1007/s10853-018-2952-6>.
- [51] F. Soleimanl, A. Nezamzadeh-Ejhieh, Study of the photocatalytic activity of CdS-ZnS nano-composite in the photodegradation of rifampin in aqueous solution, *J. Mater. Res. Technol.* 9 (6) (2020) 16237–16251, <https://doi.org/10.1016/j.jmrt.2020.11.091>.
- [52] D.A. Collu, C. Carucci, M. Poludi, D.F. Parsons, A. Salis, Aurivillius Oxides Nanosheets-Based Photocatalysts for Efficient Oxidation of Malachite Green Dye, *Int. J. Mol. Sci.* 23 (2022) 5422–5439, <https://doi.org/10.3390/ijms23105422>.
- [53] G.R. Vaz, A. Clementino, J. Bidone, M.A. Villetti, M. Falkembach, M. Batista, P. Barros, F. Sonvico, C. Dora, Curcumin and quercetin-loaded nanoemulsions: physicochemical compatibility study and validation of a simultaneous quantification method, *Nanomaterials* 10 (2020) 1650–1669, <https://doi.org/10.3390/nano10091650>.
- [54] M. Mehrabpour, A. Nezamzadeh-Ejhieh, S. Ghattavi, A. Ershadi, A magnetically separable clinoptilolite supported CdS-PbS photocatalyst: Characterization and photocatalytic activity toward Cefotaxim, *Appl. Surf. Sci.* 614 (2023) 156252–156263, <https://doi.org/10.1016/j.apusc.2022.156252>.
- [55] A. Nezamzadeh-Ejhieh, Z. Banan, Kinetic investigation of photocatalytic degradation of dimethyl disulfide by zeolite A containing nano CdS, *Iran. J. Catal.* 2 (2012) 79–83.
- [56] M. Farsi, A. Nezamzadeh-Ejhieh, A coupled Cobalt(II) oxide-Silver Tungstate nano-photocatalyst: Moderate characterization and evaluation of the photocatalysis kinetics towards methylene blue in aqueous solution, *Polyhedron* 219 (2022) 115823–115834, <https://doi.org/10.1016/j.poly.2022.115823>.
- [57] S. Ghattavi, A. Nezamzadeh-Ejhieh, A double-Z-scheme ZnO/AgI/WO₃ photocatalyst with high visible light activity: experimental design and mechanism pathway in the degradation of methylene blue, *J. Mol. Liq.* 322 (2021) 114563–114576, <https://doi.org/10.1016/j.molliq.2020.114563>.
- [58] S.A. Mirsalari, A. Nezamzadeh-Ejhieh, Focus on the photocatalytic pathway of the CdS-AgBr nano-catalyst by using the scavenging agents, *Sep. Purif. Technol.* 250 (2020) 117235–117246, <https://doi.org/10.1016/j.seppur.2020.117235>.
- [59] A.M. Caldas, D.F. Dos Santos, M.A.M. Castro, M.D. Teodoro, F.V. Motta, M. R. Bomio, Fabrication of CN-HAp heterostructures from eggshells with improved photocatalytic performance in degrading of mixing dyes under sunlight, *Mater. Sci. Semicond. Process.* 165 (2023) 107660–107673, <https://doi.org/10.1016/J.MSSP.2023.107660>.

- [60] C.H. Nguyen, C.C. Fu, R.S. Juang, Degradation of methylene blue and methyl orange by palladium-doped TiO₂ photocatalysis for water reuse: Efficiency and degradation pathways, *J. Clean. Prod.* 202 (2018) 413–427, <https://doi.org/10.1016/j.jclepro.2018.08.110>.
- [61] H.A. Abbas, R.A. Nasr, A. Khalaf, A. Al Bawab, T.S. Jamil, Photocatalytic degradation of methylene blue dye by fluorite type Fe₂Zr(2-x)W_xO₇ system under visible light irradiation, *Ecotoxicol. Environ. Saf.* 196 (2020) 110518–110527, <https://doi.org/10.1016/j.ecoenv.2020.110518>.
- [62] S. Senobari, A. Nezamzadeh-Ejhieh, A p-n junction NiO-CdS nanoparticles with enhanced photocatalytic activity: A response surface methodology study, *J. Mol. Liq.* 257 (2018) 173–183, <https://doi.org/10.1016/j.molliq.2018.02.096>.